https://doi.org/10.5194/egusphere-2024-447
Preprint. Discussion started: 5 April 2024

An Air Quality and Boundary Layer Dynamics Analysis of the Los Angeles Basin Area During the Southwest Urban NOx and VOCs Experiment (SUNVEx)

Edward J. Strobach[1,2], Sunil Baidar[1,2], Brian J. Carroll[1,2], Steven S. Brown[1,3], Kristen Zuraski[1,2], Matthew Coggon[1], Chelsea E. Stockwell[1], Lu Xu[4,5], Yelena L. Pichugina[1,2], W. Alan Brewer[1], Carsten Warneke[1], Jeff Peischl[1,2], Jessica Gilman[1], Brandi McCarty[1,2], Maxwell Holloway[1,2], and Richard Marchbanks[1]

[1]NOAA Chemical Sciences Laboratory, Boulder, CO 80309, USA
[2]Cooperative Institute for Research in Environmental Sciences, University of Colorado Boulder, Boulder, CO 80309, USA
[3]Department of Chemistry, University of Colorado Boulder, Boulder, CO 80309, USA
[4]Department of Energy, St. Louis, MO 63130, USA
[5]Department of Environmental and Chemical Engineering, Washington University at St. Louis, St. Louis, MO 63130, USA

Correspondence: Edward J. Strobach (edward.strobach@noaa.gov)

Abstract. The NOAA Chemical Sciences Laboratory (CSL) conducted the Southwest Urban NO_x and VOCs Experiment (SUNVEx) to study emissions and the role of boundary layer (BL) dynamics and seabreeze (SB) transitions on the time evolution of coastal air quality. The study presented focuses utilizes remote sensing and in situ observations in Pasadena, California.

Investigations of the synoptic conditions during days when O_3 was greater than 70 ppb led to the identification of high pressure conditions and an overall reduction in BL height throughout the day as being primary dynamical factors responsible for enhanced ozone. Enhanced trapping of pollutants at night resulted in reduced O_3 and increased NO_x (titration), while trapping during the day coincided with a simultaneous decrease in NO_x and increase in VOCs that promoted favorable O_3 conditions. To evaluate micrometeorological impacts, we selected a day when O_3 exceeded 70 ppb during a SB, used empirical mode decomposition to isolate higher frequency variations (micrometeorology), and developed a multivariate spectral coherence mapping (MSCM) technique using the Ricker wavelet to study the role of BL growth and SB transitions on the evolution of air quality measurements. The extraction of time-scales from chemistry and dynamics scaleograms led to a quantitative evaluation of dynamical contributions from BL growth and a SB transition. A statistical evaluation of chemistry data during August 2021 during BL growth supported findings from the case study, but with the caveat of SB interactions with land BL and complex chemical reactions contributing to the scatter distribution caused by day-to-day variation.

1 Introduction

Understanding the regional air quality and meteorological conditions in the Los Angeles (LA) basin has been a research interest for decades as a result of historically high pollution levels that have affected the area (Warneke et al., 2012). Reductions in

https://doi.org/10.5194/egusphere-2024-447
Preprint. Discussion started: 5 April 2024

precursor emissions has led to a declining trend in ozone (O_3) over the period extending from the 1960s up to the 21st century (Parrish et al., 2016). Since 2010, however, O_3 levels have not decreased further, despite continued declines in precursor emissions as evident in the annual maximum 8-hr average O_3 hovering around 100 ppb.

Most recent efforts in isolating the emissions responsible for the secondary formation of O_3 in the LA basin have found a wide range of emissions that include vehicles, volatile chemical products and biogenics as sources of O_3 precursors. Ryerson et al. (2013) found that carbon monoxide (CO), nitrogen oxides (NO_x), and volatile organic compounds (VOCs) were dominated by vehicular emissions. Gu et al. (2021) found that the top 10 VOCs were strongly influenced by traffic. Comparisons between weekend versus weekday emissions highlighted the important role of NO_x on O_3 formation since most of the "heavy-duty trucking" occurred on weekdays (Nussbaumer and Cohen, 2020). The isolation of alkenes from VOC measurements has highlighted motor vehicles as being an important source while at the same time underscoring the complex relationship between alkenes and hydroxyl radicals (OH) (de Gouw et al., 2017; Hansen et al., 2021). Hasheminassab et al. (2014) determined that vehicle emissions were the second most important source to $PM_{2.5}$, slightly behind secondary nitrates. However, a study in 2018 found that sources other than vehicular emissions related to pesticides, cleaning products, and personal care products (i.e., volatile chemical products–VCPs) contributed to twice the amount of VOCs compared to vehicular emissions, thus pointing to a recent shift in the dominant emission sources contributing to O_3 precursors (McDonald et al., 2018).

Other studies have highlighted different factors responsible for poor air quality. Gu et al. (2021) demonstrated that "greening" a city can increase biogenic VOCs, which could have unintended consequences for O_3 production. Muñiz-Unamunzaga et al. (2018) determined that halogen and sulfer-based compounds can modify O_3 and NO_x concentrations in coastal environments spurred by changes in OH chemistry and the HO_x (or RO_x) cycle. Nussbaumer and Cohen (2021) noted that warmer days (and nights) can lead to elevated VOC abundance, which often, but not always, coincides with conditions associated with high pressure ridging and stagnant condtions. Thus, in the case of the latter, understanding the broader meteorological conditions and the boundary layer (BL) evolution becomes important when addressing changes in atmospheric chemistry and air quality.

Composite analyses of different types of large-scale patterns have often shown stagnant high pressure as being an ideal condition for poor air quality (e.g., Lai and Cheng, 2009; Zhou et al., 2018; Nauth et al., 2023). However, the study by Nauth et al. as well as others (e.g., Peterson et al., 2019; Wang et al., 2019) have shown that interactions between different air masses, blocking patterns, and the pressure pattern arrangement (regardless of high or low pressure) can also lead to poor air quality episodes. While the latter two are larger-scale in nature, the interaction between air masses can be large-scale, mesoscale, or both. For instance, Nauth et al. (2023) found that synoptic northwesterly flows and the simultaneous development of a seabreeze (SB) from the south enhanced O_3 as the two flows merged to form a convergence line over the New York city area. Their results confirm findings from previous studies examining locally generated sea and bay breezes (e.g., Banta et al., 2005; Loughner et al., 2014). In the LA basin, modeling and observational studies have highlighted the role of mesoscale transport from SBs penetrating inland, resulting in a more complex set of chemical reactions that stem from the mixing of air between marine and terrestrial BLs (Lu and Turco, 1995; Wagner et al., 2012).

In addition to SBs generated by strong thermal constrasts between the LA basin and the coastal ocean are impacts from the complex topography to the north and east that alter the flow field as differential heating across terrain slopes generate upslope

https://doi.org/10.5194/egusphere-2024-447
Preprint. Discussion started: 5 April 2024

and downslope winds that can modify or interact with a developing SB (Pérez et al., 2020). Langford et al. (2010) found that upslope flow within the BL and forcing conditions favoring westerly flow above the BL can lead to significant transport out of the LA basin into the free troposphere through a phenomenon known as BL venting (Loughner et al., 2014). However, it is not clear how common the case described by Langford et al. is, and what combination of forcing conditions associated with SB development, background synoptic pressure gradient, and topgraphically driven flows are required to prevent transport out of the LA basin and subsequently poor air quality conditions. Thus, although we may know the factors responsible for mesoscale and large-scale forcing, we do not necessarily know how different wind regimes will interact and modify the BL dynamics. Furthermore, local impacts from urban development adds to the dynamical complexity in the form of the well-documented urban heat island (UHI) effect, which can modify SB propagation (Yoon-Hee et al., 2016) while at the same time alter the wind profile structure in the form of the urban wind island (UWI) effect (Droste et al., 2018; Baidar et al., 2020).

To address questions related to the role of dynamics on air quality in the LA basin, the NOAA Chemical Sciences Laboratory (CSL) deployed instrument payloads during August 2021 in an effort known as the Southwest Urban NOx and VOCs Experiment (SUNVEx). Instruments featuring in situ chemistry/meteorology and a Stationary Doppler lidar On a Trailer (StaDOT) were stationed in Pasadena, CA, while a mobile component was deployed to survey the regional air quality and BL dynamics. Here, we focus on data collected at Pasadena and evaluate the broader conditions observed during the month of August as well as an examination of BL growth and SB transitions on the finer scale features observed in air quality measurements. The close proximity of stationary systems in Pasadena allowed the characterization of local temporal changes in air quality and dynamics observations with the aid of a wavelet technique to determine the fine structure characteristics associated with BL dynamics within variable time series, while a mapping technique was developed to quantitatively examine the variability between independent measurements to understand dynamical linkages to air quality evolution. Results highlighting BL transitions and the role of BL growth, in particular, have major implications in air quality modeling since it is those situations where models tend to struggle (Sastre et al., 2015), and represents a key area that the authors aim to address as part of this work. Furthermore, the techniques developed in this study allow a quantitative analysis of the fine structure variability of air quality and BL dynamics observations as well as variable interdependencies during BL transitions, which, to the authors' knowledge, has never been done at this level of detail.

The remainder of the study is as follows. Section 2 describes the data used in the study and data processing methods. For data processing methods, we adopt a wavelet technique to isolate the local characteristics of the data time series after the removal of the diel cycle using empirical mode decomposition (EMD) so that maximum normalized scaleograms of multiple variables can be compared using a method that we call the Multivariate Spectral Coherence Mapping (MSCM) technique. Section 3 presents an analysis of the large-scale changes in air quality and dynamics measurements spanning the month of August. A case study is chosen and discussed in Section 4 that describes the dynamical evolution that took place on 16 August 2021, and the role that BL transitions and SB development had on air quality evolution. Section 5 expands upon analyses conducted in Section 4 by analyzing the impact of BL growth on the temporal variations in air quality and dynamics measurements during August. Conclusions with a description of study limitations and a path forward is left for Section 6. Appendices A and B describe

https://doi.org/10.5194/egusphere-2024-447
Preprint. Discussion started: 5 April 2024

algorithmic techniques for spectral mapping scaleograms through a variable ranking approach and the modeling of the BL height during the growth phase given the spectral structure of different data time series, respectively.

2 Data and Methods

Observations in Pasadena, CA featuring DL and in situ chemistry/meteorology payloads are presented in the Data section along with details of the High Resolution Rapid Refresh (HRRR) model used to describe the regional conditions. Other data used include the O_3 measurements from the AIRNOW network (https://www.AIRNOW.gov/) overlaid against output from the HRRR.

A methods section is dedicated to the application of a Ricker wavelet to stationary measurements after the removal of the time varying mean signal and the development of the Multivariate Spectral Coherence Mapping (MSCM) technique to compare the temporal likeness between multiple variables.

2.1 Data

2.1.1 Stationary Doppler lidar On a Trailer (StaDOT)

The StaDOT is a stationary DL that was deployed in Pasadena, CA (Stationary Doppler lidar On a Trailer–StaDOT) to measure winds spanning 05 August 2021 through 02 September 2021. Wind profile measurements (direction and speed) were derived from conical scans at 15, 35, and 60-degree elevation angles. The shallower 15-degree elevation angle resulted in higher resolution winds closer to the surface of about 20 m that decreased to 67 m at a height of 6000 m as the elevation angle increased. The time it took to perform conical scans was 3.5 minutes, with each revolution resulting in 120 azimuthal angles and a line of sight (LOS) velocity measurement at a 2 Hz resolution.

Following conical scans were vertical stares to measure vertical winds over a 11.5-minute period, which were used to derive vertical velocity variance, skewness, and kurtosis. Other products that were available included the signal-to-noise (SNR) ratio and the derivation of BL heights using the fuzzy logic approach from Bonin et al. (2018). The total time to complete a scan cycle was 15 minutes, thus representing the time resolution between horizontal and vertical wind measurements.

2.1.2 NO_2, NO_x, O_x, and Meteorology Measurements

in situ measurements of NO_x, NO_y, and O_x were conducted at the Caltech campus in Pasadena, CA using a 10-meter inlet tower. Three different instruments were employed, including a cavity ringdown spectroscopy (CRDS) instrument, a laser-induced fluorescent (LIF) instrument, and a commercial O_3 analyzer (TECO, Thermo Environmental Instruments, model 49c). The CRDS instrument, which has been described previously (Fuchs et al., 2009; Rollins et al., 2020; Washenfelder et al., 2011; Wild et al., 2017), consisted of four channels. NO_2, NO_x, O_x, and NO_y measurements were observed by directly measuring NO_2 using a 405 nm laser, following chemical and thermal conversions for the NO_x, O_x and NO_y species. Excess O_3 was introduced to ambient NO to convert it to NO_2 for the NO_x measurement, while excess NO was added to ambient O_3 to

https://doi.org/10.5194/egusphere-2024-447
Preprint. Discussion started: 5 April 2024

convert it to NO_2 for the O_x measurement. A heated inlet (T = 650 °C) was employed to thermally dissociate NO_y to NO and NO_2, where excess O_3 was again added to convert NO to NO_2 for the NO_y measurement. Data was collected at 1 Hz, and the accuracy of the measurements ranged from 3-5% for NO, NO_2, and NO_x, and 12% for NO_y. The LIF instrument, previously described by Rollins et al. (2020), directly measured NO at 1 Hz with an uncertainty of 6-9% and a limit of detection of 1 ppt. This two-channel instrument converted NO_2 to NO using a blue light converter for the NO_x measurement.

The data obtained from the three instruments were consolidated into a merged file, accessible online at S. (2021). The combined datasets prioritized the most direct instrument measurements when available. For NO_2, the CRDS data took precedence, with data from the LIF instrument filling in any dataset gaps. In the case of the NO_x data, NO data from LIF combined with NO_2 from the CRDS instrument was used when both were available, the CRDS data was used when the LIF instrument was inactive, and vice versa. O_3 data primarily came from the TECO instrument, except for the early campaign period when the CRDS O_3 data was used. NO_y was exclusively measured by the CRDS instrument, and this dataset remained independent of the other instruments. The uncertainty for each species depended on the instrument that measured the data and is also reported in the merge file. For the NO_x data, where NO from the LIF instrument combined with NO_2 from the CRDS instrument, propagation of error was employed to represent the uncertainty in both measurements.

A separate instrument payload to measure in situ meteorology was installed at CalTech. Measurements included temperature, pressure, relative humidity, wind speed, and wind direction recorded at a 1-minute time resolution. In this study we consider only temperature, pressure, and relative humidity since we rely on winds from the DL.

2.1.3 VOC Measurements

VOC mixing ratios were monitored using a Vocus proton-transfer-reaction time-of-flight mass spectrometer (PTR-ToF-MS, Krechmer et al., 2018). The PTR-ToF-MS was operated as described by Coggon et al. (2023). Briefly, ambient air was sampled through a ≈1 meter Teflon tube and VOC mixing ratios were measured at 1 Hz. Instrument background were determined every 2 hr by sampling a platinum catalyst heated to 350 °C. Mixing ratios were determined for small oxygenates (ethanol, methanol, acetone, acetaldehyde, methyl vinyl ketone + methacrolein), C6-C9 aromatics, biogenic VOCs (isoprene, monoterpenes), and nitriles (acetonitrile, benzonitrile) using gravimetrically-prepared standards. These VOCs have reported uncertainties of 20%. Sensitivities for other masses reported by the PTR-ToF-MS were estimated by the methods described by Sekimoto et al. (2017) and have uncertainties greater than 50%. Here, we report total VOCs as the sum of PTR-ToF-MS mixing ratios, which is used in analyses later in the manuscript.

2.1.4 High Resolution Rapid Refresh

To describe the meteorological conditions when evaluating the 16 August case study, we use the hourly output from version 4 (v4) of the 3 km High-Resolution Rapid Refresh (HRRR) model. HRRRv4 includes notable improvements to the Mellor-Yamada-Nakashini-Niino (MYNN) BL scheme related to subgrid-scale (SGS) clouds, a 36-member ensemble used for data assimilation to address uncertainty in the "initial conditions and model physics" to improve representativeness of complex flow environments, the inclusion of radar observations to improve the representation of clouds, predictions of wildfire smoke

https://doi.org/10.5194/egusphere-2024-447
Preprint. Discussion started: 5 April 2024

transport, and modifications to radiative transfer from SGS clouds. Also included is the 9 soil-layer Rapid Update Cycle (RUC) land surface model and the aerosol-aware Thomson-Eidhammer microphysics scheme. More details related to HRRRv4 can be found in Dowell et al. (2022).

When evaluating the regional conditions, we defined a plotting domain encompassing the LA basin, topography to the north and east, and the coastal Pacific Ocean along the shoreline defining one of the geographical borders outlining the LA basin. The broader synoptic conditions are also described with links to synoptic maps.

2.2 Methods

2.2.1 Empirical Mode Decomposition (EMD)

A time varying signal represented as a superposition of scales containing localized changes in the frequency structure can be decomposed via empirical mode decomposition (EMD) and represented as distinct intrinsic mode functions (IMFs) of a finite number. Pioneered by Huang and Wu (2008) to study nonlinear waves, the decomposition into IMFs is an integral component of the Hilbert-Huang Transform (HHT) to address the nonstationarity and nonlinearity of a signal. In this study, the EMD portion of the HHT is used to separate observables into IMFs and a residual.

There are two requirements when constructing IMFs: 1) the number of extrema and zero crossings must equal or differ at most by one, and 2) the mean of the envelope tracing local minima and maxima is identically zero (an example of this procedure can be found in Figure 2 from Huang and Wu (2008)). Incorporating these requirements as conditions into an algorithm through an iterative "sifting" approach enables the separation of N IMFs whose spectral characteristics range from a high-to-low frequency structure. The high frequency structure is isolated first in the sifting process and removed before the next IMF is determined. Since the higher frequency content has been separated, then the subsequent IMFs will contain lower frequency content. Eq. (1) represents the decomposition of an arbitrary signal, $x(t)$, into a summation of IMFs ($x_i'(t)$) and a residual ($x_r(t)$)

$$x(t) = x_r(t) + \sum_{i=1}^{N} x_i'(t) \tag{1}$$

The residual represents the portion of the signal that is either constant or features a time varying mean that did not satisfy one of the two requirements above. The number of modes varies depending on the data collected, the type of observations or variables being processed, or the resolution of measurements, and can be determined by the limit that $x_i'(t)$ goes to zero, i.e.,

$$\lim_{x_i'(t) \to 0 \; \forall \; t} i = N + 1 \tag{2}$$

The number of IMFs, N, is truncated according to Eq. (2), where the summation of IMFs is used in Sections 4 and 5 to isolate variations due to the diel cycle from the fine structure variability. Thus, we use the summation of IMFs defined by Eq. (3) when conducting a wavelet analysis in frequency space and when applying the Multivariate Spectral Coherence Mapping (MSCM)

https://doi.org/10.5194/egusphere-2024-447
Preprint. Discussion started: 5 April 2024

technique that is described later.

$$\tilde{x}(t) = \sum_{i=1}^{N} x_i'(t) = x(t) - x_r(t) \tag{3}$$

Figure 1a shows a 24-hour period of measured O_3 (blue) and the residual (red). The residual represents the diurnal structure of O_3, while Figure 1b represents the summation of IMFs as defined by Eq. (3). The positive and negative values in $\widetilde{O}_3$ represent the fine scale variability superimposed on the diurnal trend.

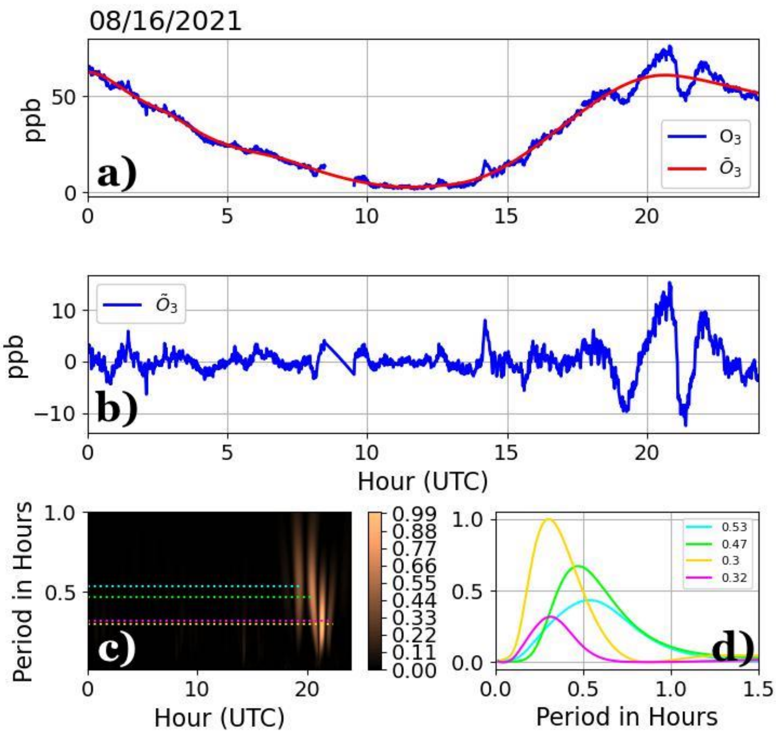

Figure 1. a) Measurements of O_3 (blue) overlaid with the portion of measurements driven by the diel cycle (red), b) the variability of O_3 after the removal of the time varying mean, c) a scaleogram using results from b) with different wavelet dilations overlaid with dotted lines highlighting peaks in the scaleogram, and d) the maximum normalized power spectrum density (PSD) color-matched with dotted lines in c). The legend in d) represents the temporal width associated with the dominant extremum in the PSD.

2.2.2 The Ricker Wavelet and the scaleogram

In order to analyze the fine structure variability of chemistry and meteorological measurements to understand the role of BL transitions, we apply a wavelet across 24-hour blocks of data spanning the diel cycle. For this analysis we chose the continuous

https://doi.org/10.5194/egusphere-2024-447
Preprint. Discussion started: 5 April 2024

Ricker wavelet defined by Eq. (4)

$$\psi\left(\frac{t-b}{\tau}\right) = \frac{2}{\sqrt{3\tau}\pi^{1/4}}\left(1-\left(\frac{t-b}{\tau}\right)^2\right)e^{\frac{-(t-b)^2}{2\tau^2}} \tag{4}$$

where τ is the width or dilation of the wavelet, and b is the position of the wavelet along the data time series. The wavelet is symmetrical and is derived from normalizing the negative of the second derivative of a Gaussian function with respect to time, thus leading to a structure that resembles a sombrero.

The summation of IMFs in Eq. (3) is convolved with Eq. (4) to obtain a power spectrum, $\widetilde{W}_\psi(\tau,b)$, at a given dilation, τ, via Eq. (5)

$$\widetilde{W}_\psi(\tau,b) = \int_{-\infty}^{\infty} \tilde{x}(t)\psi\left(\frac{t-b}{\tau}\right)dt \tag{5}$$

Increasing or decreasing the dilation leads to isolating the slow or rapidly varying portions of the signal, respectively, which when grouped together produces a 2D spectrum dependent on dilation (τ) and the position of the wavelet (b), the result of which is joined together to produce a scaleogram as shown in Figure 1c. The scaleogram represents the maximum normalized power spectrum density (PSD) with respect to time as the wavelet is translated across the time series (b–x-axis), and with respect to the temporal width of variations teased out by the dilation of the wavelet, τ (dilation–y-axis), where the maximum normalized PSD is simply represented as

$$\widetilde{\chi}_\psi(\tau,b) = \frac{\widetilde{W}_\psi(\tau,b)}{max\left(\widetilde{W}_\psi(\tau,b)\right)} \tag{6}$$

2.2.3 Isolating Peaks in the Scaleogram

Since each time within a scaleogram corresponds to a series of real-valued coefficients derived from changing the wavelet dilation, then it is possible to determine the temporal width (or dilation) associated with a maximum PSD at each time step (i.e., $max\left(\widetilde{\chi}_\psi(\tau,b)\right) = \widetilde{\chi}_\psi(\tau_{max},b) \rightarrow \widetilde{\chi}_\psi(b)$). Once the maximum PSD is found at each time step, then the time-ordered output can be sorted from increasing to decreasing maximum PSD (i.e., $\widetilde{\chi}_\psi(b) \rightarrow \widetilde{R}_\psi(k) = \widetilde{R}_\psi^k$) to isolate the peaks that stand out from the rest of the dataset, where k replaces b as the time-independent sorted index. By defintion, the sorted output for a single variable being processed through a wavelet transform and normalized by the maximum PSD will begin with a value of 1 according to Eq. (6). From there, the output of the sorted array decreases toward zero. We identify significant peaks in $\widetilde{R}_\psi^k$ by comparing neighboring peaks via Eq. (7),

$$\Gamma = \sum_{\substack{k \\ \Gamma > 0.5 \vee \widetilde{R}_\psi^{k+1} \geq 0.25}} \frac{\widetilde{R}_\psi^{k+1}}{\widetilde{R}_\psi^k} \tag{7}$$

where the conditions within the summation terminate the algorithm if the subsequent peak within the sorted array is less than half the value of the larger adjacent peak, or if $\widetilde{R}_\psi^{k+1}$ is less than or equal to 0.25. The conditions were chosen based on trial and error, and are necessary if we are only interested in isolating clear signatures linked to micrometeorological dynamics.

https://doi.org/10.5194/egusphere-2024-447
Preprint. Discussion started: 5 April 2024

Figure 1c includes overlays of dotted lines that identify the peaks determined as significant using the method outlined above, while Figure 1d shows the corresponding $\widetilde{\chi}_{\psi}(b)$ color-matched with dotted lines in c). The PSD associated with $\widetilde{\chi}_{\psi}(b)$ in Figure 1d resembles a gamma distribution-like character, with peaks in $\widetilde{\chi}_{\psi}(b)$ decreasing from 0.53 to 0.3 hours.

2.2.4 The Multivariate Spectral Coherence Mapping (MSCM) Technique

To compare the PSD between variables, we use the maximum normalized PSD defined by Eq. (6), which results in a range of values between 0 and 1 as shown in the color-scale in Figure 1c. This is necessary since we are comparing the spectral structure of variables with unlike units, and since the variability may not change proportionately. Furthermore, ensuring that the normalized power spectrum distribution falls between 0 and 1 allows the mapping of multiple power spectrum distributions onto a single scaleogram with values also falling between 0 and 1. For two variables, $\widetilde{\chi}_{\psi}^{1}$ and $\widetilde{\chi}_{\psi}^{2}$, we multiply and raise the product to the 1/2 to define a type of cross-spectrum between two sets of observations. In a general sense, we can extend the operation to an arbitrary number of variables with Eq. (8)

$$\widetilde{C}^{L}(\tau,b) = \left(\prod_{j=1}^{L} \widetilde{\chi}_{\psi}^{j}(\tau,b)\right)^{1/L} \tag{8}$$

where L is an arbitrary number of variables and j represents the variable number index. The superscript in $\widetilde{\chi}_{\psi}^{j}(\tau,b)$ does not represent a power, but rather a power spectrum associated with a variable assigned to index j. Eq. (8) is basically the geometric mean of power spectra for L variables normalized by their respective maximum power. Though not a measure of coherence in the traditional sense, which uses the formal cross-spectrum definition between variables after being processed through a Fourier transform, the mapping of normalized power spectra highlights temporal widths within the dataset where variables exhibit similar spectral variability, thus revealing instances between datasets where there is structural coherence. Furthermore, this method is slightly different than wavelet coherence methods (e.g., Grinsted et al., 2004) in that the maximum PSD is used over the standard deviation when normalizing, a smoothing operator is not used, and we extend the analysis to any number of variables, not just two.

Eq. (8) provides the advantage of being able to determine variables that vary together in time, thus potentially enabling the determination of conversion relationships between atmospheric compounds and the role of BL dynamics on time changes in chemistry measurements. We call this method the Multivariate Spectral Coherence Mapping (MSCM) technique since we are able to produce scaleograms for an arbitrary number of variables that vary in time. Additionally, we can order scaleograms according to spectral likeness with a reference variable. For instance, if we define a reference variable, $\widetilde{\chi}_{\psi}^{m_0}$, and compute all possible variable pairings (2 variables) with the remaining $M-1$ variables that are left, then we have a vector space defined by

$$\widetilde{\boldsymbol{C}}^{2} = \{(\widetilde{\chi}_{\psi}^{m_0}\widetilde{\chi}_{\psi}^{m_1})^{1/2}, (\widetilde{\chi}_{\psi}^{m_0}\widetilde{\chi}_{\psi}^{m_2})^{1/2}, ..., (\widetilde{\chi}_{\psi}^{m_0}\widetilde{\chi}_{\psi}^{m_{M-1}})^{1/2}\} \tag{9}$$

Each pairing within the vector space in Eq. (9) can be summed with respect to time and dilation using Eq. (10)

$$S_m = \sum_{i=1}\sum_{l=1} \widetilde{C}_m^2(\tau_i, b_l) \tag{10}$$

https://doi.org/10.5194/egusphere-2024-447
Preprint. Discussion started: 5 April 2024

where m represents the index associated with an arbitrary variable pairing in Eq. (9), i is a dummy index for dilation, and l is the time index. The $M-1$ summations of Eq. (9) via Eq. (10) can be used to sort the array of S_m's and indices in descending order, i.e.,

$$max(\widetilde{\boldsymbol{C}}^2) = \{(\widetilde{\chi}_{\psi}^{m_0}\widetilde{\chi}_{\psi}^{n_1})^{1/2}, (\widetilde{\chi}_{\psi}^{m_0}\widetilde{\chi}_{\psi}^{n_2})^{1/2}, ..., (\widetilde{\chi}_{\psi}^{m_0}\widetilde{\chi}_{\psi}^{n_{M-1}})^{1/2}\} \quad (11)$$

where n has replaced m in Eq. (9) as a result of being maximum sorted. The result above can be expressed in general terms for an arbitrary number of variable groupings. Eq. (11) is used to determine groupings of two (or more) variables that share the strongest spectral likeness using calculations in Eq. (10). Thus, the order of scaleograms presented in Figures 8 and 9 is based on a decreasing sum from a) to i). An appendix is included below that discusses the algorithmic procedure for optimal ordering of variables based on maximum pattern likeness of M variables (Appendix A).

3 Results

Most of the measurements taken simultaneously by the DL and in situ instruments in Pasadena, CA occurred during August 2021. Figure 2 shows a) O_3, b) NO_x/NO_y, c) VOCs, d) $\sum_i VOC_i/NO_x$, e) O_x, and f) $PM_{2.5}$. Figure 3 shows a) temperature, b) relative humidity, c) BL-averaged wind speed, d) BL-averaged wind shear, e) BL height, and f) pressure. Both Figures 2 and 3 are overlaid with a 25 ppb contour of NO_x and a 70 ppb contour of O_3 in magenta and gray, respectively. We chose an O_3 threshold of 70 ppb to define O_3 exceedance, realizing that the national air quality standard definition for O_3 exceedance applies to O_3 averaged over 8-hour periods rather than to instantaneous measurements. For chemistry observations, we included NO_x and VOCs because of the well documented influence on O_3 production, NO_x/NO_y to identify whether emissions were recent since it takes time for NO_x to oxidize into other compounds (e.g., HONO, PAN, etc.), the ratio between total VOCs to NO_x to highlight NO_x-sensitive versus VOC-sensitive regimes, the summation of O_3 and NO_2 (i.e., O_x) to examine whether interactions between NO_2 and O_3 were conserved, and $PM_{2.5}$ as an air quality metric. Meteorological measurements were chosen to examine the thermodynamic and dynamic characteristics under varying synoptic conditions.

The diurnal structure of O_3 in Figure 2a is demonstrated by a minimum at night and a maximum during the day that closely resembles the diurnal temperature structure in Figure 3a. The morning transition that is driven by increased surface temperature accelerates chemical reactions of most atmospheric compounds (Pusede et al., 2014) while increased downward solar short-wave flux promotes photochemistry that leads to O_3 production. Periods where O_3 exceeded 70 ppb occurred in clusters during 08/05-08/12, 08/14-08/16, and 08/22-08/29, or roughly half of the month of August, and occurred on both weekdays and weekends.

A strong overlap between periods of O_3 exceedance and increased (decreased) temperature (relative humidity) in Figure 3a(b) during the day, especially in the latter part of the month, is illustrated by the gray 70 ppb O_3 contour. During instances of O_3 exceedance, BL heights in Figure 3e were shallower while BL-averaged winds appeared slightly reduced in the hours following sunrise (Figure 3c). Other meteorological fields such as BL-averaged wind speed shear (∂ws/∂z–Figure 3d) and surface pressure (Figure 3f) did not exhibit clear contrasting patterns between O_3 exceedance and non-exceedance days. Figure

https://doi.org/10.5194/egusphere-2024-447
Preprint. Discussion started: 5 April 2024

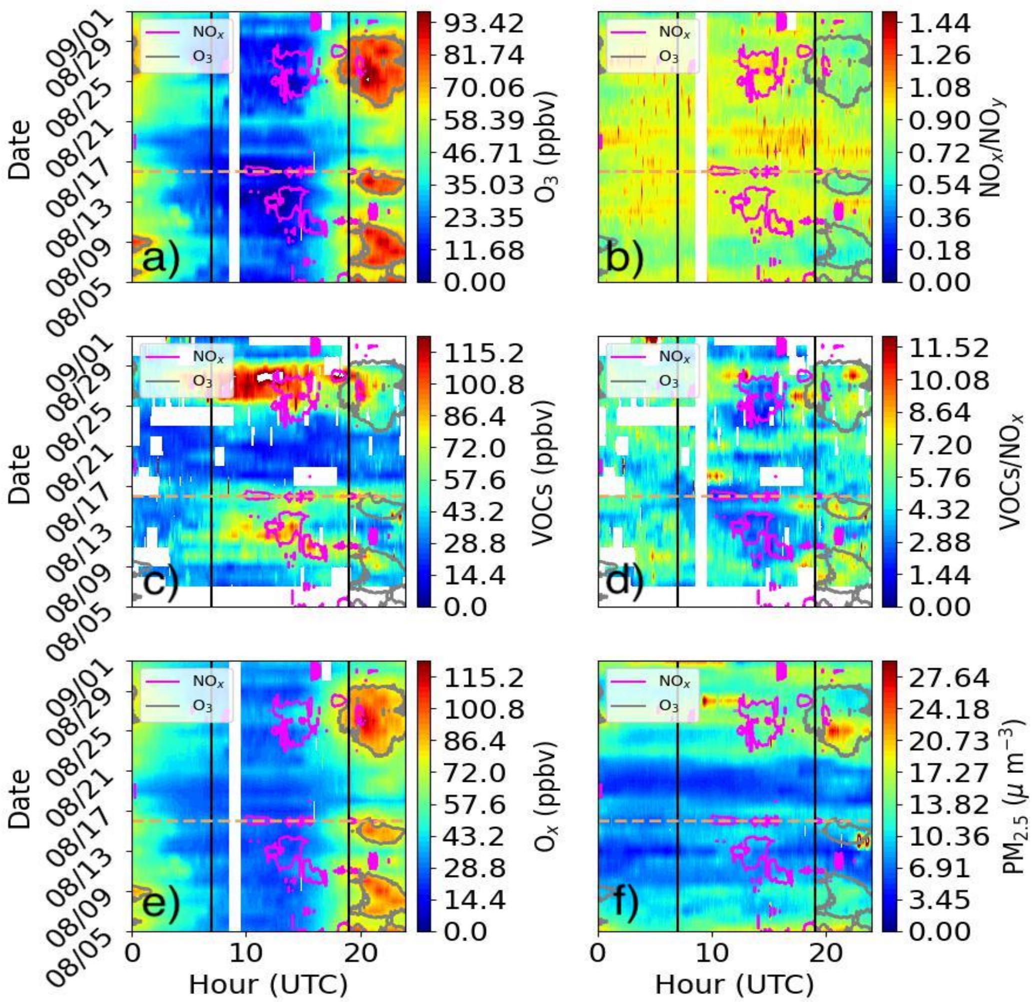

Figure 2. in situ observations of a) O_3, b) NO_x/NO_y, c) VOCs, d) $\sum_i VOCs/NO_x$, e) O_x, and f) $PM_{2.5}$ in Pasadena, CA overlaid with a 25 ppb NO_x contour in magenta and a 70 ppb O_3 contour in gray. Included is a day chosen for a case study (gold dashed line). Vertical black lines denote midnight (7 UTC) and solar noon (19 UTC).

2b shows decreases in NO_x/NO_y, particularly during O_3 exceedance days, that overlapped with increased $VOCs/NO_x$ ratios in excess of 5 as shown in Figure 2d. $VOCs/NO_x$ ratios in excess of 5 are known to favor increased O_3 production that can ultimately lead to O_3 exceedance as evident by the 70 ppb contour encapsulating relatively high $VOCs/NO_x$ ratios (Seinfeld and Pandis, 2016). The simultaneous decrease in NO_x/NO_y and increase in $VOCs/NO_x$ is further exemplified by Figure 2c, which shows VOCs remaining elevated while NO_x significantly depleted into the day. The depletion of NO_x and increase in VOCs into the day coincides with large increases in O_3 and O_x in Figure 2e. Instances of elevated VOCs, and thus elevated O_3,

https://doi.org/10.5194/egusphere-2024-447
Preprint. Discussion started: 5 April 2024

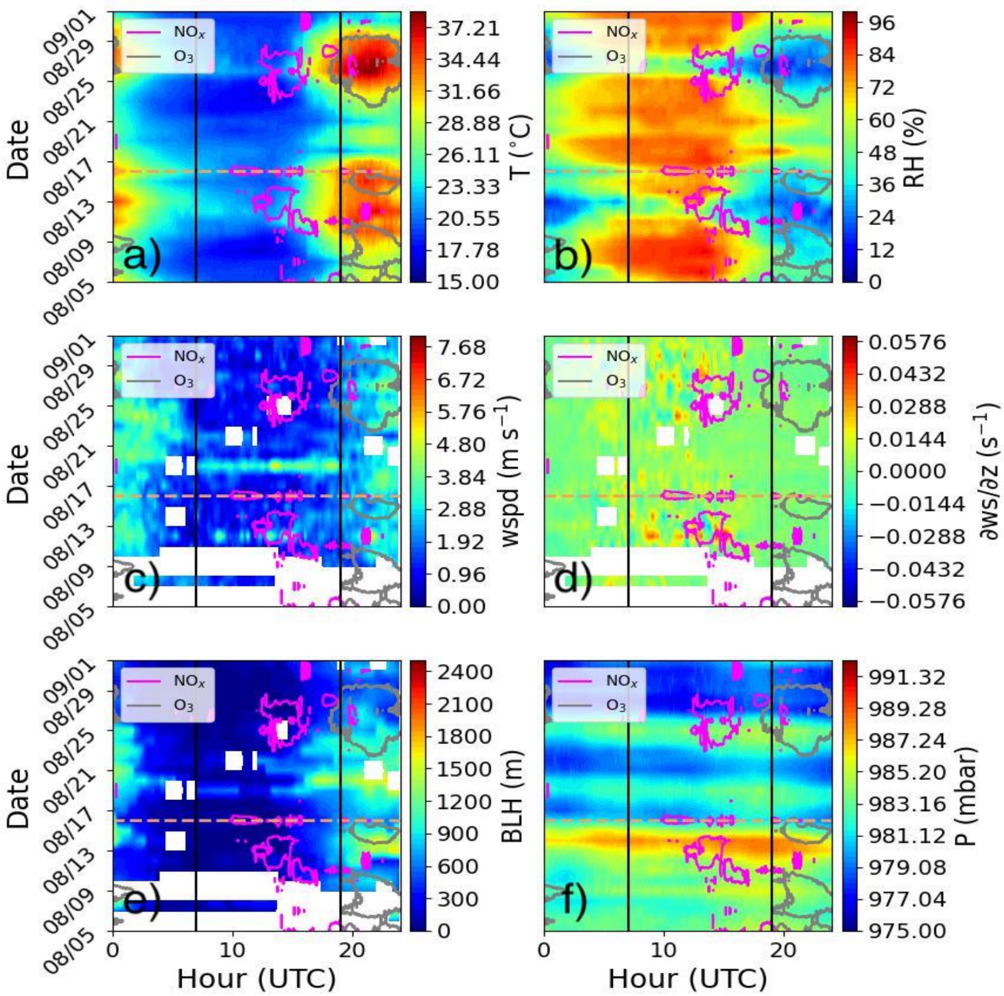

Figure 3. Observations of a) surface temperature, b) surface relative humidity, c) BL-averaged wind speed, d) BL-averged wind shear, e) BL height. and f) surface pressure in Pasadena, CA overlaid with a 25 ppb NO_x contour in magenta and a 70 ppb O_3 contour in gray. Included is a day chosen for a case study (gold dashed line). Vertical black lines denote midnight (7 UTC) and solar noon (19 UTC).

occurred during days that were more polluted overall as indicated by $PM_{2.5}$ in Figure 2f, which also coincided with reductions in BL height (Figure 3d). Some studies have shown VOC concentrations increase with temperature (e.g., Nussbaumer and Cohen, 2021), which may partially explain the longevity of VOCs well into the afternoon despite convective BL mixing.

Studying the evening conditions leading up to O_3 exceedance days is also very important. Figure 2a shows relatively lower O_3 concentrations during evenings that preceded O_3 exceedance days after August 12th. Furthermore, evenings with relatively low O_3 coincided with increased NO_x as a result of increased NO_2 and NO (magenta contour in Figure 2a), increased

https://doi.org/10.5194/egusphere-2024-447
Preprint. Discussion started: 5 April 2024

NO_x/NO_y (Figure 2b–regardless of whether or not an evening preceding an O_3 exceedance day), and increased VOCs (Figure 2c). Interestingly, the large increases in NO_x during those evenings led to a substantial reduction in the VOCs-to-NO_x ratio well below 5 that overlaps with the 25 ppb contour of NO_x in Figure 2d, suggesting the relative importance of NO at the destruction of O_3 and the formation of NO_2 as exemplified by a nearly constant O_x overnight. The set of reactions that pertain to the NO_x cycle in R1-R3

$$NO + O_3 \rightarrow NO_2 + O_2 \quad \text{(R1)}$$

$$NO_2 + h\nu \rightarrow NO + O(^3P) \quad \text{(R2)}$$

$$O(^3P) + O_2 + M \rightarrow O_3 + M \quad \text{(R3)}$$

describe the role of NO as a sink to O_3 at night (R1) while photochemical reactions govern the dissociation of NO_2 (R2) and the production of O_3 as radical oxygen combines with molecular oxygen (R3). However, as discussed in the previous paragraph, the reaction equations are incomplete since increases in O_x and the VOCs-to-NO_x ratio suggest a more complex set of chemical reactions with VOCs that lead to O_3 exceedance events that cannot be described by R2 alone, which includes the coupling of the NO_x and RO_x via R4-R7 rewritten from Wang et al. (2017)

$$HO_2 + NO \rightarrow OH + NO_2 \quad \text{(R4)}$$

$$RO_2 + NO \rightarrow RO + NO_2 \quad \text{(R5)}$$

$$OH + RH + O_2 \rightarrow RO_2 + H_2O \quad \text{(R6)}$$

$$RO + O_2 \rightarrow HO_2 + carbonyls \quad \text{(R7)}$$

Examining the BL height in Figure 3e during the evening and comparing with elevated NO_x in Figure 2b shows relatively shallower BL heights compared to evenings where NO_x was low (i.e., during evenings where BL was slightly deeper). Reductions in the nighttime BL are usually accompanied by light wind conditions, reduced wind shear, and cooler temperatures; however, only wind speed shear exhibited a clear contrasting pattern, with increased shear preceding high O_3 days when the evening BL was deeper and vice-versa (Figure 3d). Nevertheless, a reduction in BL height, which is a result of increased static stability, can promote the removal of O_3 by NO_x titration within a reduced mixing volume under calm winds.

https://doi.org/10.5194/egusphere-2024-447
Preprint. Discussion started: 5 April 2024

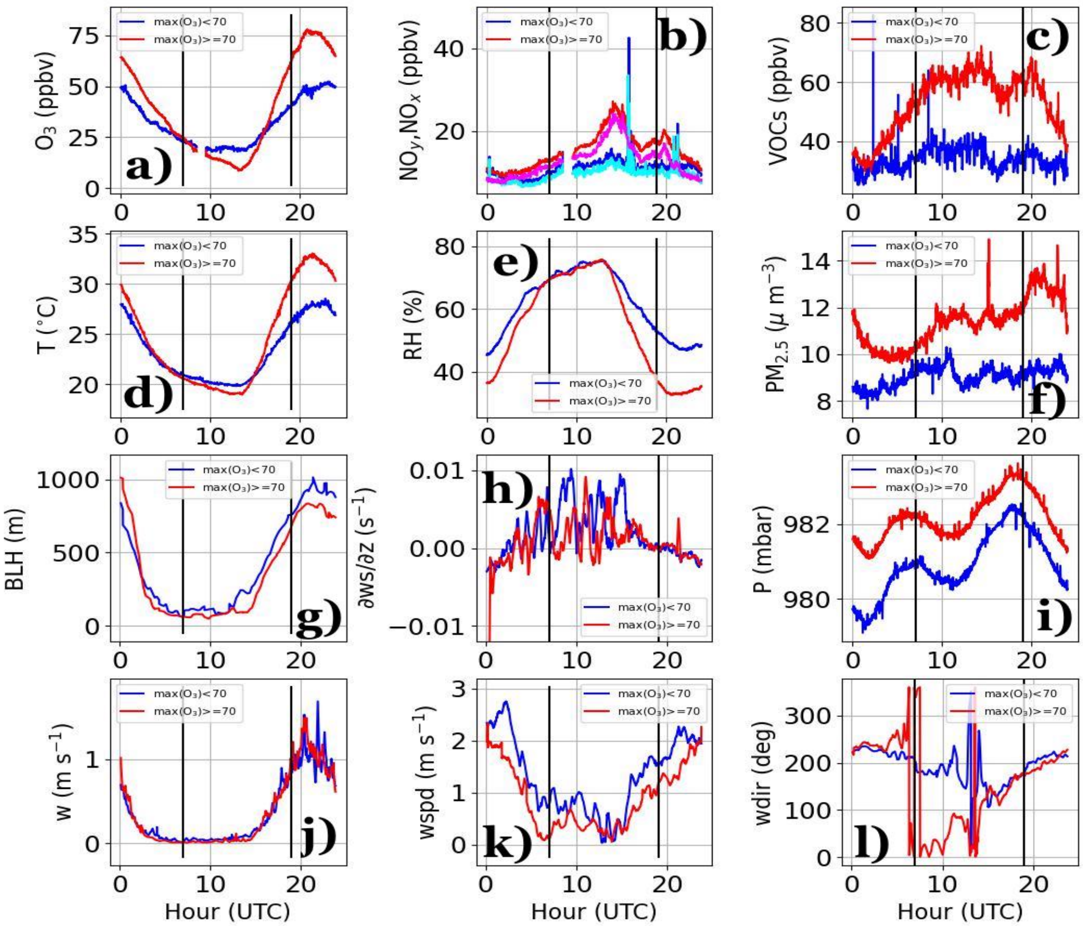

Figure 4. a) O_3, b) NO_x (red and blue) and NO_y (magenta and cyan), c) VOCs, d) surface temperature, e) surface relative humidity, f) $PM_{2.5}$, g) BL height, h) BL-averaged wind shear, i) surface pressure, j) BL-averaged vertical velocity, k) BL-averaged wind speed (wspd), and l) BL wind direction (wdir) derived by averaging the BL-averaged wind components (u,v) grouped by days where O_3 exceeded (red or magenta–b)) and did not exceed (blue or cyan–b)) 70 ppb. Vertical black lines denote midnight (7 UTC) and solar noon (19 UTC).

Figure 4 synthesizes results from Figures 2 and 3 by grouping data on days where O_3 exceeded 70 ppb (red) and during days where O_3 did not reach 70 ppb (blue). Much of what was discussed in Figures 2 and 3 is confirmed in Figure 4. However, Figure 4 reveals additional information about the BL structure and large-scale conditions that was too difficult to discern in Figures 2 and 3. For instance, periods of high pressure (Figure 4i) coincided with increased temperature (Figure 4d), reduced

https://doi.org/10.5194/egusphere-2024-447
Preprint. Discussion started: 5 April 2024

relative humidity (Figure 4e), and a reduction in BL height (Figure 4g) and BL-averaged wind speed (Figure 4k) during the day, while at night, the surface temperature was cooler, BL heights were shallower, and BL-averaged winds and wind speed shear (Figure 4h) was reduced. The reduction in wind speed and cooler temperatures at night when BL heights were lower supports increased static stability as suggested in the previous paragraph. While little can be ascertained from the BL-averaged vertical velocity in Figure 4j, the wind direction in Figure 4l was northerly when surface pressure was high and southwesterly when surface pressure was low during nights preceding days where $O_3 \geq 70$ ppb and $O_3 < 70$ ppb, respectively, before converging to a southwesterly wind into the afternoon hours that is supportive of onshore flow.

It is important to note that increased surface pressure, which is known to promote fair weather conditions and periods of stagnation (Zhang et al., 2017), coincided with polluted conditions as shown by elevated $PM_{2.5}$ (Figure 4f), an increase in VOCs throughout the day (Figure 4c), and an increase in NO_x (red) and NO_y (magenta) during the night (Figure 4b). This ultimately led to a decrease in O_3 at night when conditions were NO_x rich, and an increase in O_3 during the day as VOC concentrations remained high. Furthermore, increased pollution during O_3 exceedance days occurred contemporaneously with lower BL heights, weaker wind conditions, and increased temperature. While increased surface temperature is usually accompanied by deeper BL heights, increased surface pressure coincides with an increase in large-scale subsidence that could lead to warming aloft, thereby increasing static stability at the height of the BL layer inversion. The relative strength of the superadiabatic layer near the surface and the strength of the BL inversion act as controls on the BL height through positive and negative buoyancy, respectively. While it is clear that the BL structure is different between low ($O_3 < 70$ ppb) and high ($O_3 \geq 70$ ppb) pressure days, it must also be kept in mind that an increase in temperature could lead to higher use of cooling facilities that can promote an increase in pollution (Zhang et al., 2017).

Other notable features in Figure 4 are found in the nighttime wind speed shear (Figure 4h), spikes in NO_x and NO_y (Figure 4b), and the semi-diurnal pattern in surface pressure. The increased wind speed shear at night across the BL is a mechanism for enhanced mechanical production of turbulence that can deepen the BL and weaken stability, thus supporting the concomitant increase in BL heights in the evening previously mentioned (Figure 4g). The spikes in NO_x occurred some time after sunrise (16 UTC) and around the time period SBs arrived (21 UTC or 2p PT). However, these spikes could represent exceptional events that are not representative of all days and yet stand out due to a relatively small sample size. The semi-diurnal pressure pattern occurred thoughout the whole month of August. Local peaks in pressure occurred at 7 UTC (midnight PT) and 19 UTC (solar noon PT), respectively, with a general increase in pressure that began around sunset (around 0 UTC). Other panels in Figure 4 do not feature this semi-diurnal trend; however, the troughs in pressure at 1 UTC (6p PT) and 11 UTC (4a PT) occurred near the evening and morning transitions, respectively.

4 Evaluating the Micrometeorological Role on Air Quality, a Case Study – 16 August 2021: Pasadena, CA

In the previous section we evaluated the diurnal structure of O_3, NO_x, and VOCs during August 2021 and their relationship to the large-scale meteorology and BL structure. We now turn to a case study highlighting the convective growth phase superimposed with a SB that occurred on 08/16/21 (i.e., gold dashed line in Figures 2 and 3) to study the micrometeorological

https://doi.org/10.5194/egusphere-2024-447
Preprint. Discussion started: 5 April 2024

impacts on air quality measurements. While a SB was observed most days during the month of August – winds transitioned to a southwesterly regime with BL wind enhancement (refer to Figure 3c and Figure 4k for wind speed increases and Figure 4l for wind direction shift around solar noon, 19 UTC) – we chose this case study to examine the interesting oscillations observed in NO_x and O_3 that were 180 degrees out of phase following the arrival of the SB (discussed below), and to evaluate the utility of the MSCM under different BL transitions that occurred over a single diurnal period.

4.1 Synoptic and Regional Conditions

The LA basin was largely free of major large-scale meteorological features. The 500 mb upper air map (https://weather.uwyo.edu/cgi-bin/uamap?REGION=naconf&OUTPUT=gif&TYPE=obs&TYPE=an&LEVEL=500&date=2021-08-16&hour=12) shows a tropical cyclone far to the south and a semi-permanent offshore high pressure over the Pacific ocean, east of Hawaii. The extra-tropical patterns farther to the north do not extend to the LA basin. The surface analysis map (https://www.wpc.ncep.noaa.gov/archives/web_pages/sfc/sfc_archive_maps.php?arcdate=08/16/2021&selmap=2021081612&maptype=namussfc) reveals a more complex dynamical set-up, with significant flow modifications over the eastern United States as tropical cyclone Fred moves into the Gulf of Mexico. Over the southwest portion of the United States is a mix of local high and low pressure systems that exhibit a wave-like character behind a dryline. Two weak low pressure centers are in relatively close proximity to the LA basin at this time, with the low east of the LA basin adjacent to the alternating low and high pressure centers positioned behind the dryline.

Figure 5 shows the HRRR output of BL height (shading), near-surface winds (white barbs), and 500 mb geopotential height (gray contours). Overlaid on maps are observations of O_3 (shaded circles) from AIRNOW and the Pasadena site location as indicated by a magenta star. BL heights in the morning were generally low (sub-kilometer) across the LA basin and across large swaths of elevated terrain, although local increases in BL height in excess of 2 km are evident at 17 UTC (10a PT) (Figure 5b). The winds over the LA basin during the morning hours were weak, with little in the way of a discernible wind pattern. O_3 concentrations were generally low across the LA basin with some increases to the north and east of Pasadena over elevated terrain. Winds over the coastal ocean were nearly uniform and followed a cyclonic pattern along the coastline.

By the afternoon, O_3 began to increase near the coastline and across the LA basin. BL heights also increased in the LA basin, with some areas locally increasing in BL depth to about 1.2 km. Farther north into elevated terrain, BL heights increased from 1.5 km at 12p PT to 2.5 km at 2p PT. A southwesterly flow that developed in the early afternoon penetrated farther into the LA basin towards elevated terrain by 2p PT, with a clear drop in BL height across coastal areas as marine BL air propagated into the region. Enhancements in O_3 concentrations between 19 and 21 UTC (12p and 2p PT) are demonstrated more clearly east of Pasadena, with concentrations in excess of 100 ppb. The arrival of the SB according to the DL, as shown in the next section in Figure 6b, occurred roughly at 19 UTC (12p PT), which is in agreement with what is seen in the HRRR output. The enhancement in O_3 east of Pasadena occurred along the leading edge of southwesterlies and a gradient in BL height as a result of onshore flow associated with a SB, which can form a convergence line. The enhancement of O_3 from AIRNOW along the leading edge of southwesterlies by the HRRR corroborates findings from Nauth et al., which also found poor air quality conditions within the vicinity of a convergence line on SB days. However, it is important to note that the BL height

https://doi.org/10.5194/egusphere-2024-447
Preprint. Discussion started: 5 April 2024

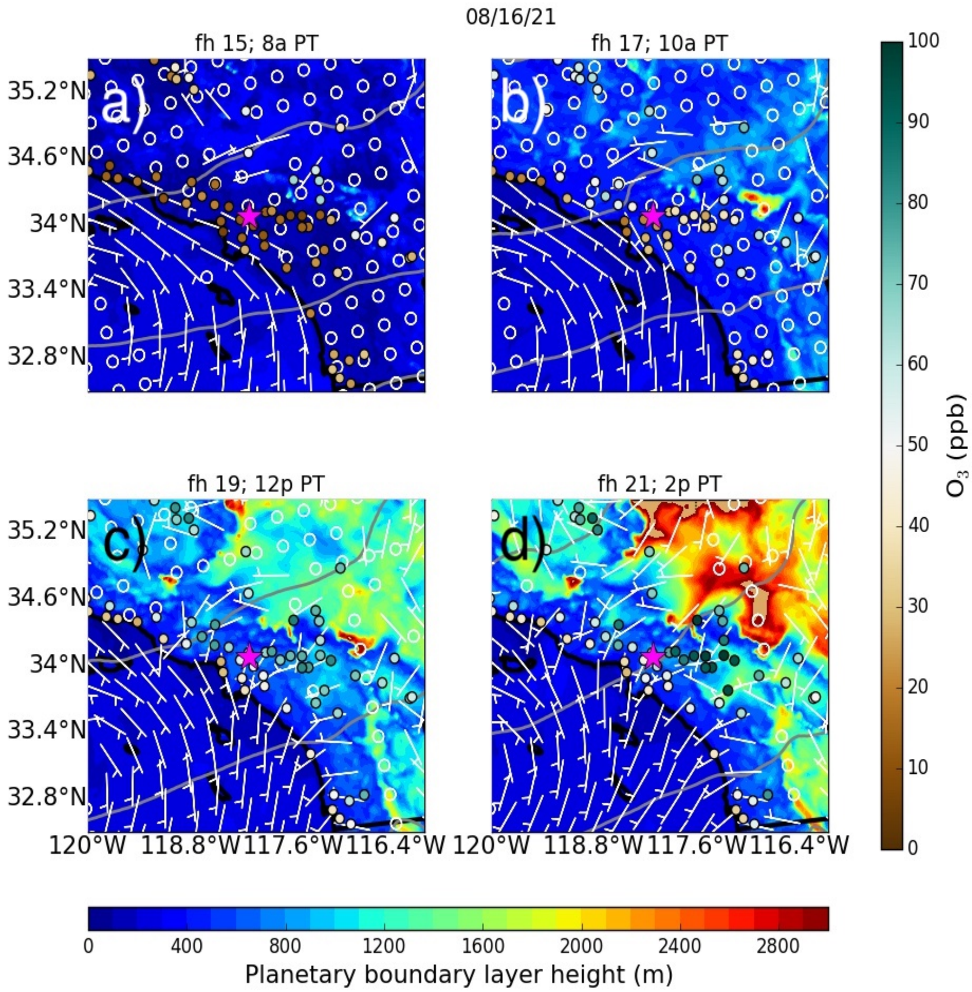

Figure 5. HRRR output of BL height (shading), near-surface winds (white wind barbs), 500 mb geopotential height (gray contours), AIRNOW O_3 observations (circles–shaded), and the Pasadena site location (magenta star) during a) 15 UTC (8a PT), b) 17 UTC (10a PT), c) 19 UTC (12p PT), and d) 21 UTC (2p PT).

gradient occurred across elevated terrain, where the backdrop of the mountains can act as a natural barrier to SB penetration, thereby leading to elevated pollution levels in situations where flow propagation is limited by the potential energy associated with ascending elevated terrain and because of the flow interaction with neighboring pressure patterns (low to the east).

https://doi.org/10.5194/egusphere-2024-447
Preprint. Discussion started: 5 April 2024

4.2 in situ Chemistry and Doppler Lidar Observations

Figure 6 shows the horizontal wind speed, wind direction, and vertical velocity overlaid with a 1 m s^{-1} vertical velocity contour and BL height from the DL (a-c); and in situ NO_x, VOCs, O_3, O_x, and temperature (d) in Pasadena, CA. A shallow BL developed during the evening (less than 60 m) with weak easterly winds within the first 500 m that were occasionally interspersed with shallow northerly flows extending in the first 100 m from the surface. Above 500 m, winds increased and veered northwesterly. VOCs and NO_x increased into the night as the BL became shallower. The decrease in BL height also coincided with reduced temperatures and a drop in O_3. The inflected behavior between NO_x and O_3 throughout the evening is revealed by nearly constant O_x as shown in gray.

The BL morning transition began a little after 13 UTC (6a PT) as the temperature increased, the BL deepened, vertical velocities increased, and winds near the surface transitioned from northerly to southeasterly. It was at this time that O_3, NO_x, and VOC concentrations changed rapidly. The initial response in VOCs and NO_x was similar: a brief increase followed by a sharp decrease. O_3, by contrast, increased over the same time interval that NO_x and VOC concentrations decreased. Between 15 and 18 UTC (8a and 11a PT), O_3 exhibited a linear increasing trend that followed closely with surface temperature.

A second decrease in VOC concentrations around 17 UTC (10a PT) coincided with a sharp drop in NO_x and a slight lull in the BL height, and occurred simultaneously with a change in wind direction from southeasterly to southerly. At the same time, an easterly wind descended from above (gray arrows in Figure 6a-b) along with increased horizontal winds at BL top (1 km). The general pattern of descent related to background subsidence can increase the strength of the BL inversion, thus leading to increased winds riding on top of the BL after 17 UTC (10a PT) as a result of increased stability from BL top into the lower free troposphere. Furthermore, changes in the wind structure at the top of the BL covary with small fluctuations in BL height, BL winds (horizontal and vertical), and, to some extent, pollution concentrations (refer to dashed lines in Figures 6a-b,d). The increases in updraft strength (Figure 6c) coincide not only with increased winds at BL top and a transition of surface winds to southwesterly (i.e., arrival of the SB), but also bursts in wind speed that are sometimes staggered temporally with increased updraft strength. The spacing between updrafts occurs coincidently with temporal extrema in NO_x and O_3, and is related to the transport dynamics associated with the SB propagating into Pasadena, and the strong wind speed shear across the BL that promotes entrainment at the top of the BL.

The pulsing/periodic development of updrafts appears largely responsbile for the oscillations in NO_x and O_3, which are 180 degrees out of phase. Examining O_x during this time reveals small amplitudinal variations that share the same phase as O_3 (i.e., O_3 fluctuates with greater amplitude than NO_x). Unlike NO_x and O_3, VOC concentrations do not oscillate, and in fact gradually decrease as the surface temperature decreases. The decrease in surface temperature is likely related to cooler marine BL air entering Pasadena. A decrease in VOCs could be related to the introduction of an air mass with less VOCs, or as a result of interactions with unrepresented chemistry not considered in this analysis. However, as previously mentioned, the oscillations that began at the onset of the SB appear related to the micrometeorological characteristics of the BL, the changes in the mixing volume, and the chemical concentrations as air mixes and interacts within a volume containing altered an chemical distribution.

https://doi.org/10.5194/egusphere-2024-447
Preprint. Discussion started: 5 April 2024

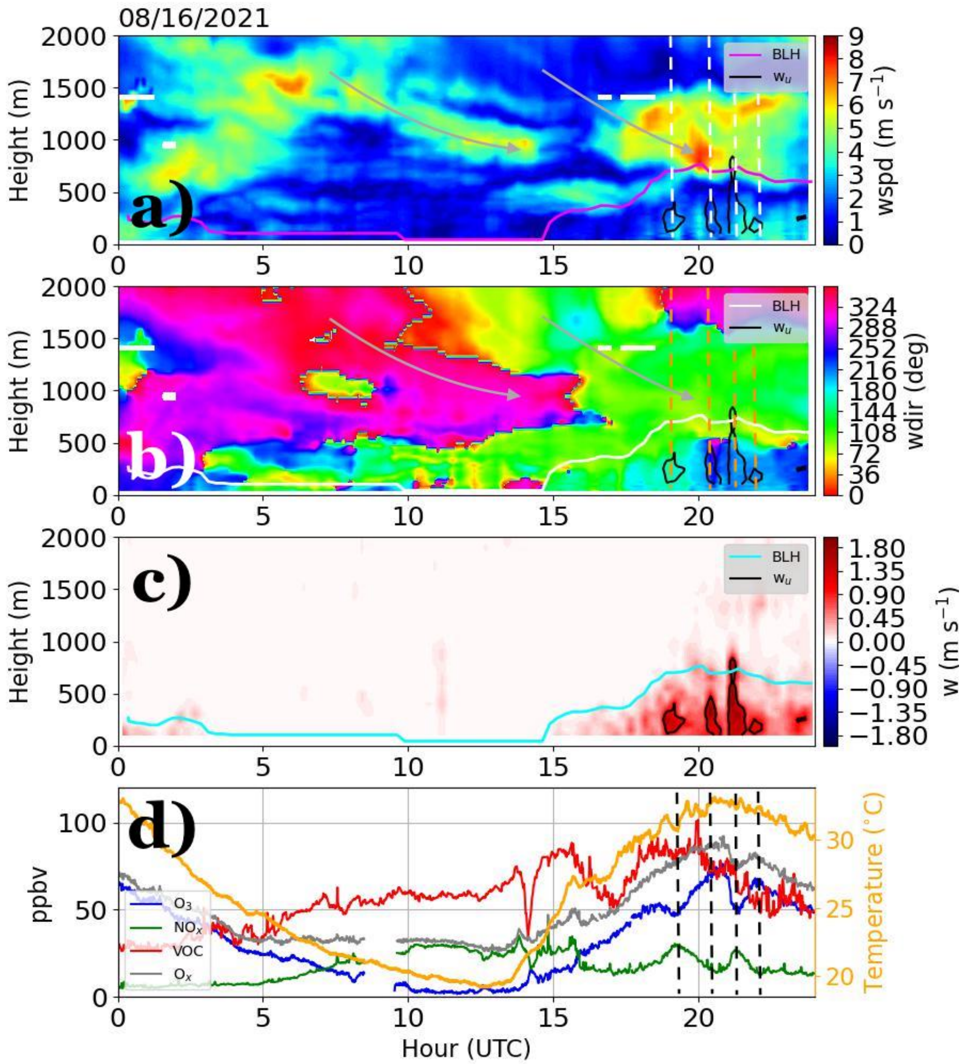

Figure 6. Profiles of a) wind speed b) wind direction, c) vertical velocity, and d) in situ O_3 (blue), NO_x (green), VOCs (red), O_x (gray), and temperature (orange) in Pasadena during 08/16/21. Overlaid in a) and b) are gray arrows indicating patterns of descent (i.e., subsidence). Contours of 1 m s^{-1} of vertical velocity are included in a)-c) along with BL height. Dashed lines intersecting the center of updrafts in a) white, b) orange, and d) black are also shown. The consistent upward vertical motion in c) is suspected to be related to the smearing of weak downward motions relative to stronger upward motions over 15-minute time intervals.

https://doi.org/10.5194/egusphere-2024-447
Preprint. Discussion started: 5 April 2024

4.3 Spectral Characteristics of Air Quality and Meteorological Variables

Changes observed in in situ chemistry measurements visually correlate with changes in the BL dynamics, especially during the growth phase of the BL and during the onset of the SB. Using techniques to remove contributions from the diel cycle, we now focus more quantitatively on the micrometeorological influence on pollution concentrations using methods described in sections 2.2.1-2.2.4.

Figure 7 shows the temporal variability of chemistry (O_3, NO_x, VOCs, and O_x–a-c, f) and meteorological (temperature, relative humidity, BL-averaged wind speed, BL-averaged wind shear, and BL height – d-e, g-i) measurements. Peaks in O_3 began at 19 UTC (solar noon) and are related to the oscillatory structure observed during the onset of the SB and as the BL height climaxed. The temporal width of extremum associated with the oscillations decreased from a half hour to 15 minutes. Similar peaks in the scaleogram during this time were found in NO_x (Figure 7b) and O_x, though the temporal variations associated with O_x was more constant and hovered around 20 minutes (Figure 7f). Other variables do not appear strongly correlated with variations in O_3 based on visual inspection.

The morning transition featured robust variability, particularly in NO_x and VOCs (Figure 7b-c). Smaller scale variability near sunrise is observed in relative humidity (Figure 7e), BL-averaged wind speed (Figure 7g), BL height (Figure 7i), and NO_x (Figure 7b) and VOCs (Figure 7c) as surface heating promotes BL growth and the erosion of the residual layer through entrainment. The micrometeorological response near the surface manifests as high frequency peaks between 5 and 30 minutes, with NO_x and VOCs exhibiting changes in concentration at a higher frequency than dynamic and thermodynamic measurements. Undoubtedly, the rapid mixing and entraining of the residual layer that initially begins across a shallow BL not only leads to adjustments in the wind speed and themodynamic vertical structure, but also the depth of the BL and the chemical concentrations that extend across the BL as air gets entrained during the BL growth phase. The temporal width of NO_x and VOCs varies less rapidly as the BL deepens, with time-scales ranging from 10 minutes at sunrise to a little over an hour as the BL reached maximum depth, and is somewhat matched by BL height variations shown in Figure 7i.

Other features in Figure 7 include small-scale variations in temperature near the time that the SB entered Pasadena; the nighttime variability in relative humidity, temperature, and wind shear during the evening transition; and larger temporal variations observed in relative humidity (Figure 7e) that increased into the evening before the onset of rapid mixing at sunrise that led to rapid changes in surface meteorology measurements.

Using the algorithmic approach outlined in Section 2.2.4 and Appendix A, we now seek variables that share spectral characteristics with O_3, NO_x, VOCs, and O_x. We avoid pairing in situations where there are strong self-correlations (e.g., O_x&O_3 and O_x&NO_x) and determine pairings with the strongest spectral similarities. Figure 8 shows the spectral structure of different variables either paired with O_3, NO_x, or VOCs–O_x did not make the list of the top 9 variable pairings. With the exception of O_3&NO_x, which was added to the plot independently, the remaining pairings are in order of structural similarity or maximum pattern likeness from b) to i). The spectral structure of O_3&NO_x in Figure 8a highlights the covariability between O_3 (Figure 7a) and NO_x (Figure 7b) during the SB transition, where only the peaks sharing similar temporal widths coincident in time stand out between the two variables. The overlapping spectral structure featuring dominant peaks (well above 0.8) is related to

https://doi.org/10.5194/egusphere-2024-447
Preprint. Discussion started: 5 April 2024

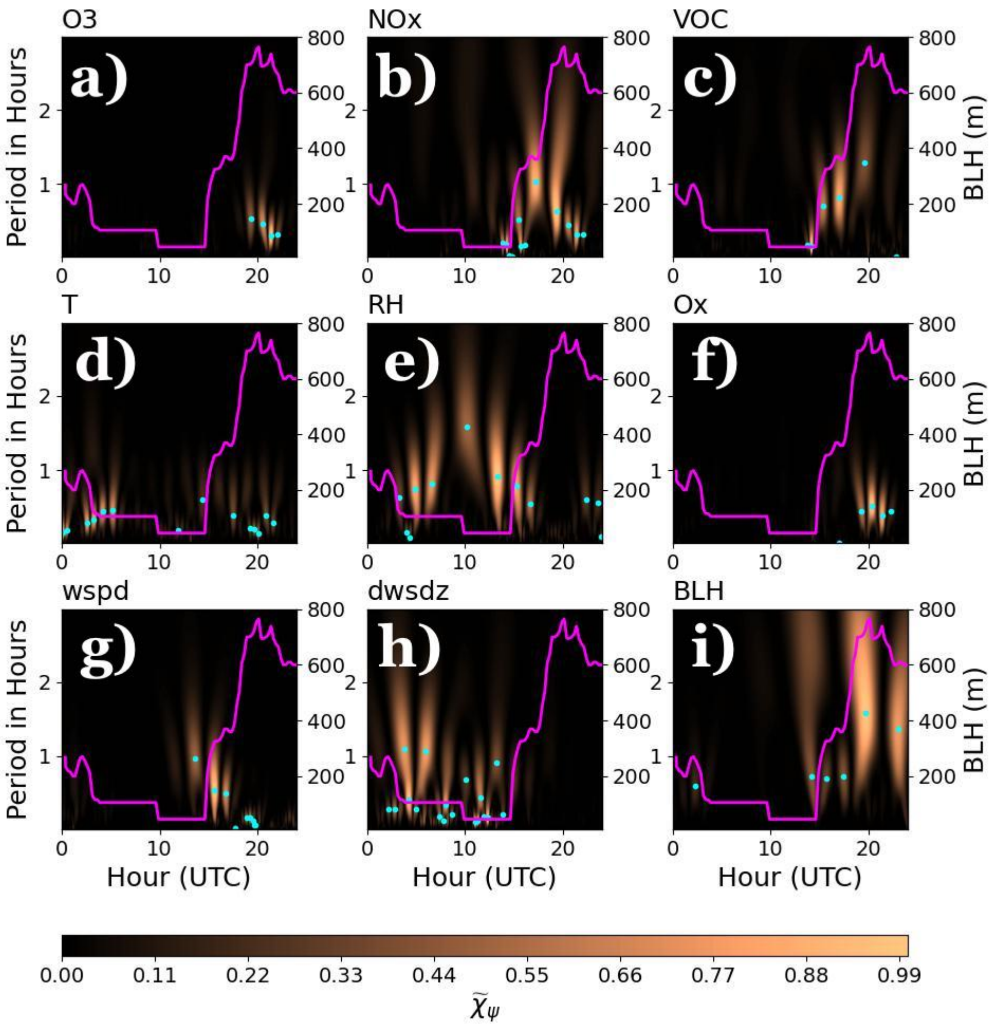

Figure 7. scaleograms of a) O_3, b) NO_x, c) VOCs, d) temperature, e) relative humidity, f) O_x, g) BL-averaged wind speed, h) BL-averaged wind speed shear, and i) BL height during 08/16/21. Overlaid on scaleograms is BL height in magenta and the location of maxima in the power spectral peaks shown by cyan dots.

the oscillations in O_3 and NO_x discussed in Figure 6d that coincide with the spacing of updrafts (Figure 6a-c). Other chemistry pairings reveal similarities between VOCs with NO_x during the growth phase of the BL. For instance, the maximum normalized PSD in Figure 8d features less rapid temporal variations in the fine structure as the BL deepens, thus hinting at the role of increased overturning time-scales associated with mixing across a deeper layer, provided that the velocity of overturning eddies does not change appreciably. The meteorological variable whose spectral structure agrees with observations from in situ chemistry the most is variations in BL height (b-c). In fact, the cross-spectra between VOCs&BL and NO_x&BL is remarkably

https://doi.org/10.5194/egusphere-2024-447
Preprint. Discussion started: 5 April 2024

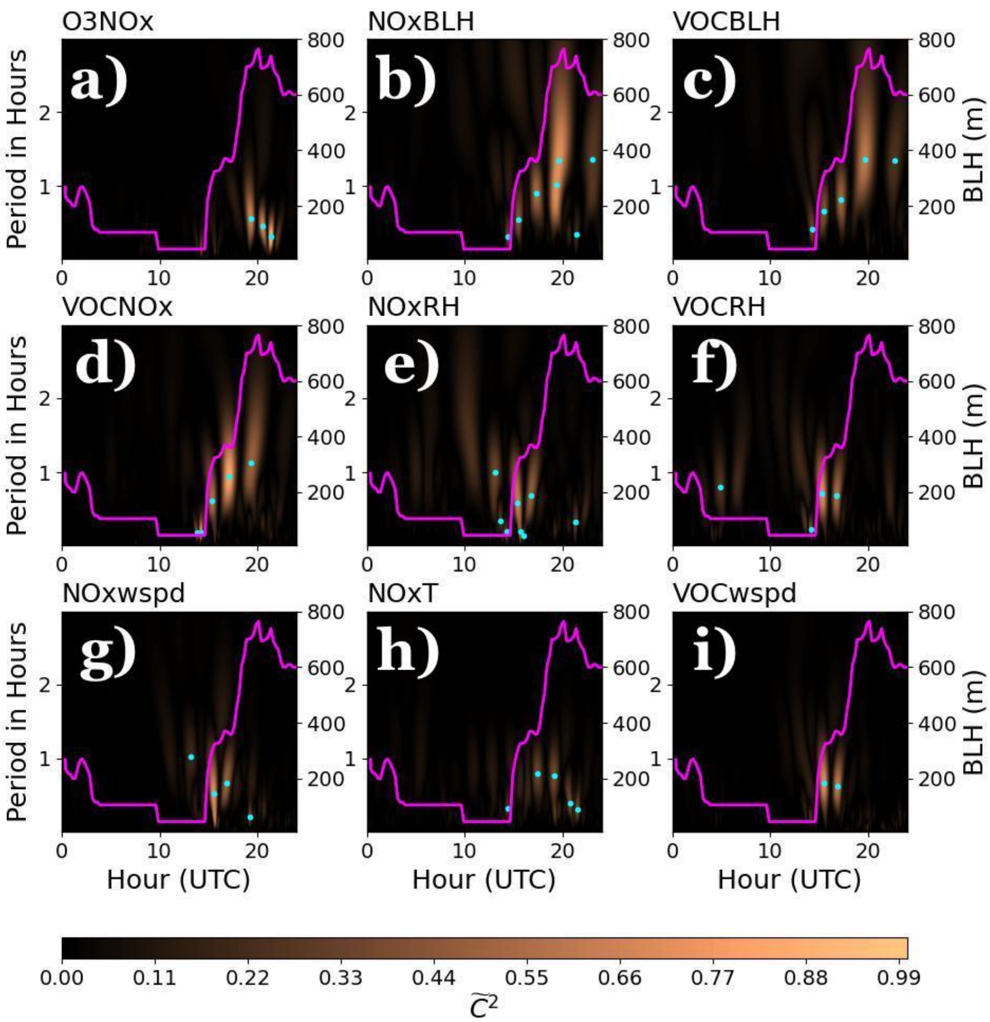

Figure 8. scaleograms of a) O_3&NO_x, b) NO_x&BL height, c) VOCs&BL height, d) VOCs&NO_x, e) NO_x&relative humidity, f) VOCs&relative humidity, g) NO_x&BL-averaged winds speed, h) NO_x&temperature, and i) VOCs&BL-averaged wind speed on 08/16/21. Overlaid on scaleograms is BL height in magenta and the location of maxima in the power spectral peaks shown by cyan dots.

similar, with the time-scale of variability ranging from 15 minutes during sunrise to about 1.25 hours as the BL climaxed. The similarity between VOCs&BL and NO_x&BL should not be too suprising, however, given the spectral structure in Figure 8d.

Temporal variability of other meteorological variables, such as relative humidity, temperature, and BL-averaged wind speed, occurred concomitantly with changes in NO_x and VOCs around sunrise. The initial growth of the BL naturally led to an adjustment in the relative humidty and wind structure as drier air and stronger winds from aloft mixed to the surface. The covariations during the initial growth phase between NO_x and VOCs with relative humidity and BL-averaged wind speed

https://doi.org/10.5194/egusphere-2024-447
Preprint. Discussion started: 5 April 2024

(Figure 8e-g, i) occurred over 5 to 45-minute periods between 15 and 17 UTC (8a and 10a PT), with pairings associated with wind speed leading to larger temporal widths (DL had coarser resolution). Faint spectral signatures are also evident in NO_x&temperature measurements that line up with temporal variations in relative humidity&BL-averaged wind speed during the initial BL growth phase and during the onset of the SB (after 20 UTC or 1p PT). The faint spectral signatures, however, must be taken lightly since a reduced PSD between two variables implies reduced coherence between the temporal structure of variables paired.

Combinations of three variables were also examined as shown in Figure 9. While interdependencies begin to reduce when grouping multiple variables, VOCs&NO_x&BL height variations in Figure 9a shows a strong dependence between these three variables during the BL growth phase according to the maximum normalized PSD, which agrees with findings in Figure 8b-d. Other combinations between three variables reveal rapid changes during the initial growth of the BL.

The spectral characteristics from Figures 7-9 highlight the role of BL growth and a SB transition on modifications to chemistry and dynamics measurements, and how the time-scale of air quality measurements changes as the BL evolves. The clearest impacts occurred during the BL growth phase. As such, we isolate variables and pairings of variables in Figures 7 and 8, respectively, that showed a decrease in time-scale as the BL height increased. Figure 10a plots cyan dots from Figures 7 and 8 (i.e., the temporal extremum) for variables and variable pairings that were sensitive to BL growth, color-coded according to the legend, and fitted using an assumed powerlaw. With the exception of NO_x, all other variables and variable pairings are in close agreement with one another. Although NO_x is an outlier, the trend for each variable and variable pairing shows an increase in temporal extremum from about 0.2 hours to a little over an hour spanning the BL growth phase. We combine the BL height reported at the time that a maximum period within scaleograms was identified during the BL growth phase, i.e.,

$$V_{\tau_{max}} = \frac{z_{BL}}{\tau_{max}} \tag{12}$$

where $V_{\tau_{max}}$ is a velocity scale. Figure 10b combines the numerator (y-axis) and denominator (x-axis) to derive the slope ($V_{\tau_{max}}$). As can be seen, the reported slopes range between 0.14 m s^{-1} to 0.21 m s^{-1}, with the weakest confidence in NO_x–all other variables correlate well with the linear fit (i.e., >0.9). These velocities are quite a bit higher compared to the slope of 0.03 m s^{-1} derived by applying a linear fit to BL height in Figure 10c. However, acknowledging that turbulent eddies inherently have vortical motion and therefore rotate air, and BL growth involves upward motion driven by convection and downward motion as the residual layer gets mixed into the growing BL, we decided to normalize the slopes from Figure 10b by 2π to account for full eddy rotations, noting that the velocity scales are too small to be resolved explicitly by the DL (Schroeder et al., 2020; Strobach et al., 2023). Adopting the 2π normalization factor and noting constant velocities derived from the slopes leads to agreement with dz_{BL}/dt during BL growth phase such that

$$\frac{dz_{BL}}{dt} \approx \frac{z_{BL}}{2\pi\tau_{max}} \tag{13}$$

Eq. (13) approximately holds for the case analyzed and represents a first order differential equation, the solution of which is exponential under the assumption that τ_{max} does not change with respect to time, i.e.,

$$z_{BL}(t) = z_{BL,0}\, e^{t/2\pi\tau_{max}} \tag{14}$$

https://doi.org/10.5194/egusphere-2024-447
Preprint. Discussion started: 5 April 2024

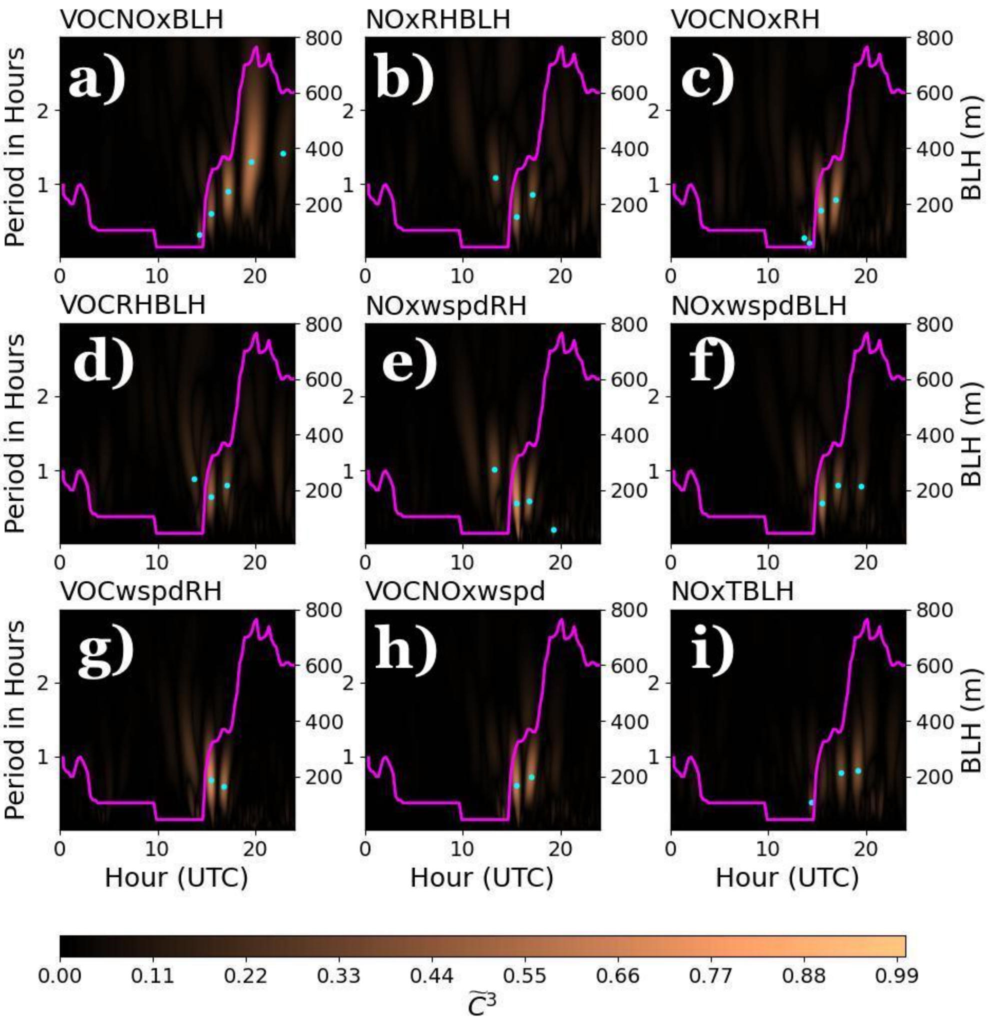

Figure 9. scaleograms of a) VOCs&NO_x&BL height, b) NO_x&relative humidity&BL height, c) VOCs&NO_x&relative humidity, d) VOCs&relative humidity&BL height, e) NO_x&BL-averaged winds speed (wspd)&relative humidity, f) NO_x&BL-averaged wind speed&BL height, g) VOCs&BL-averaged wind speed&relative humidity, h) VOCs&NO_x&BL-averaged windspeed, and i) NO_x&temperature&BL height on 08/16/21. Overlaid on scaleograms is BL height in magenta and the location of maxima in the power spectral peaks shown by cyan dots.

However, because τ_{max} changes with time, then Eq. (14) cannot be used as a valid analytical function to model the behavior of the BL. Instead, if we revisit Eq. (12), take the time derivative, carry out a series of algebraic manipulations and substitutions, integrate with respect to time, and assume that the velocity scales do not change appreciably as justified by the lines of best fit

https://doi.org/10.5194/egusphere-2024-447
Preprint. Discussion started: 5 April 2024

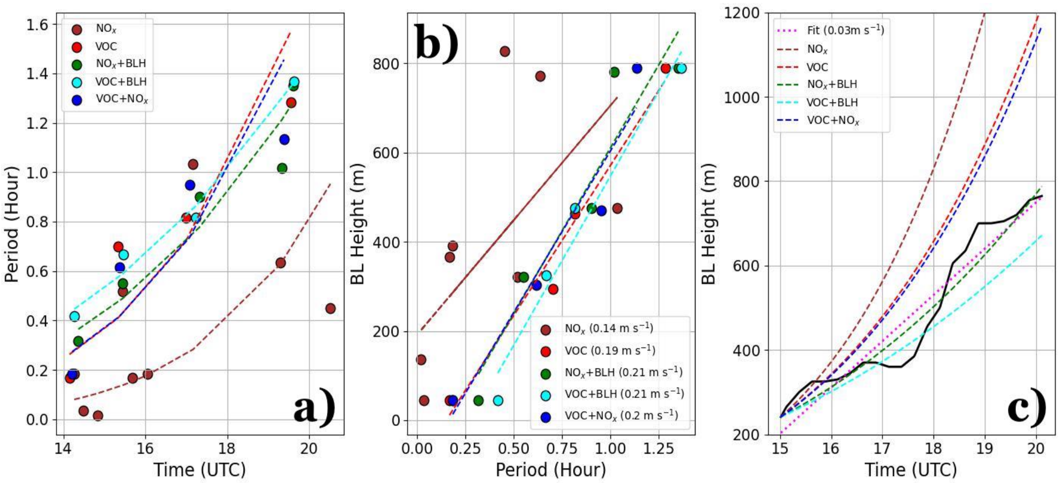

Figure 10. a) Time versus maximum period (τ_{max}), b) maximum period versus BL height, and c) time versus BL height. In a), b), and c) we overlay lines of best fit using an assumed powerlaw, linear fits, and fits using Eq. (15), respectively. A pink dotted line in c) is additionally included as a linear fit to BL height with a derived growth rate of 0.03 m s^{-1}.

in Figure 10b, then we arrive to Eq. (15)

$$z_{BL}(t) = z_{BL,0}\frac{\tau_{max}(t)}{\tau_{max,0}} \tag{15}$$

where $z_{BL,0}$ is the BL height at sunrise and $\tau_{max,0}$ is the time-scale at sunrise derived from fits in Figure 10a. A full derivation of Eq. (15) is left for Appendix B. As can be seen, the fits have a wide range of behavior, with several overestimating, one slightly underestimating, and another modeling the BL growth with strong confidence. The strong sensitivity between modeled curves is owed to the different estimates of τ_{max} between different variables and variable pairings examined and the derived power from the fits in Figure 10a. The modeled curves that closely reproduce the evolution of the BL are from τ_{max}'s derived when combining the 2D spectral structure from chemistry output with BL height variations rather than single variables alone (i.e., NO_x and VOCs). While this appears borne out of hyperdependence on BL height, we are simply using the fact that the temporal structure of NO_x and VOCs during the growth phase is highly correlated with variations in BL height rather than BL height itself. The overestimating fit lines closest to the observed BL height trend (VOCs&NO_x and VOCs) model the BL height reasonably well up to 18.5 UTC (11:30a PT) before departures between fits and the observed BL become large, which occurs approximately at the start of the SB transition. Adjustments not only in the mixing volume and the depth of the BL, but changes in chemical reactions as concentrations dilute BL air and mix free tropospheric air from above offers a possible explanation for the mismatch between observed and modeled BL height.

The results above highlight which measurements were affected by BL growth versus measurements affected during the SB. While NO_x and VOCs showed a response that scaled with the BL, NO_x and O_3 were sensitive to the dynamical evolution of the SB. Mapping the spectral structure of variables onto one another allowed an examination of shared temporal characteristics that further accentuated the role of BL on the fine structure features in pollutants during transitional periods, and allowed

https://doi.org/10.5194/egusphere-2024-447
Preprint. Discussion started: 5 April 2024

quantitative estimates of the temporal variability of measurements. However, is this finding representative of the data collected during the entire month of August? For that, we now turn to Section 5 to explore this problem more statistically.

5 BL Growth and Transitions During August 2021

Applying the methods described in 2.2.1-2.2.4 to the entire dataset allows a statistical evaluation during the BL growth phase for the month of August. We isolate the time period spanning 14 and 20 UTC (7-13 PT), identify all the dominant spectral extremum from scaleograms as discussed in Section 2.2.3, and determine how the temporal width of extrema varied with time and BL height. We consider variables and variable pairings that exhibited rapid changes during BL growth in Figures 7 and 8.

Figure 11 represents the temporal width of extremum (y-axis) versus time (x-axis) for selected variables and variable pairings. The top two rows in Figure 11 represent single variables (except Figure11f), while the bottom row represents variable pairings when identifying temporal extremum. Single variables and O_3&NO_x consist of 5 or more days that have been identified as having 4 or more temporal extremum between 14 (7 PT) and 20 (13 PT) UTC. For variable pairings on the bottom row of Figure 11 (g-i), between 2 and 3 days were identified with 4 or more temporal extremum. The lack of days identified for variable pairings prevents a robust statistical analysis, but we can still comment on the distribution of the scatter.

For single variable pairings, only NO_x and VOCs show indications of increased temporal width with respect to time. Other variables such as O_3, O_x, and relative humidity are too widely dispersed. Though NO_x and VOCs stand out more compared to other variables, the scatter is still widely dispersed, especially for NO_x. VOCs, on the other hand, feature the strongest evidence of the temporal width of extremum increasing with time. It should be noted that many of the days coincided with the arrival of a SB or onshore flow, which adds an additional layer of complexity when interpreting the statistics since BL growth will be modified by the dynamics associated with an encroaching SB. We do not expect the SB to evolve identifcally between days, but from what was found for the 16 August case study, the arrival of the SB coincided with high frequency variability in air quality measurements (recall O_3, NO_x, and O_x in Figure 7). We attempt to subjectively identify dense clusters of points in variables/variable pairings that coincide roughly with the time that onshore flow begins to occur (near 17 (10 PT) UTC). Both relative humidity (e) and VOCs (c) feature high frequency variability spanning the time that a SB was typically observed, which occurred most days during August 2021. Focusing on the scatter outside of red ovals, it is clear that the temporal width of extrema for both relative humidity and VOCs increase with time. The only variable pairing that exhibits an increase in temporal width with respect to time is NO_x&VOCs; all other variable pairings lack a discernible relationship.

Figure 12 shows the temporal width of extremum (x-axis) versus BL height (y-axis) for the same variable and variable pairings in Figure 11. For single variables (a-e), only NO_x and VOCs exhibit a general increase in the temporal width of extremum with BL height. Other variables are too widely dispersed to determine a clear relationship between BL growth and increases in the temporal width of extremum. As in Figure 11, we subjectively identify the high frequency cluster coinciding with the time period spanning the typical arrival of the SB for relative humidity (e) and VOCs (c). Ignoring the high frequency scatter points, it is clear that the temporal width of extremum for relative humidity and VOCs increase with BL height. The main cluster of points in Figure 12c that do not include the scatter within the red oval or the large temporal widths at low

https://doi.org/10.5194/egusphere-2024-447
Preprint. Discussion started: 5 April 2024

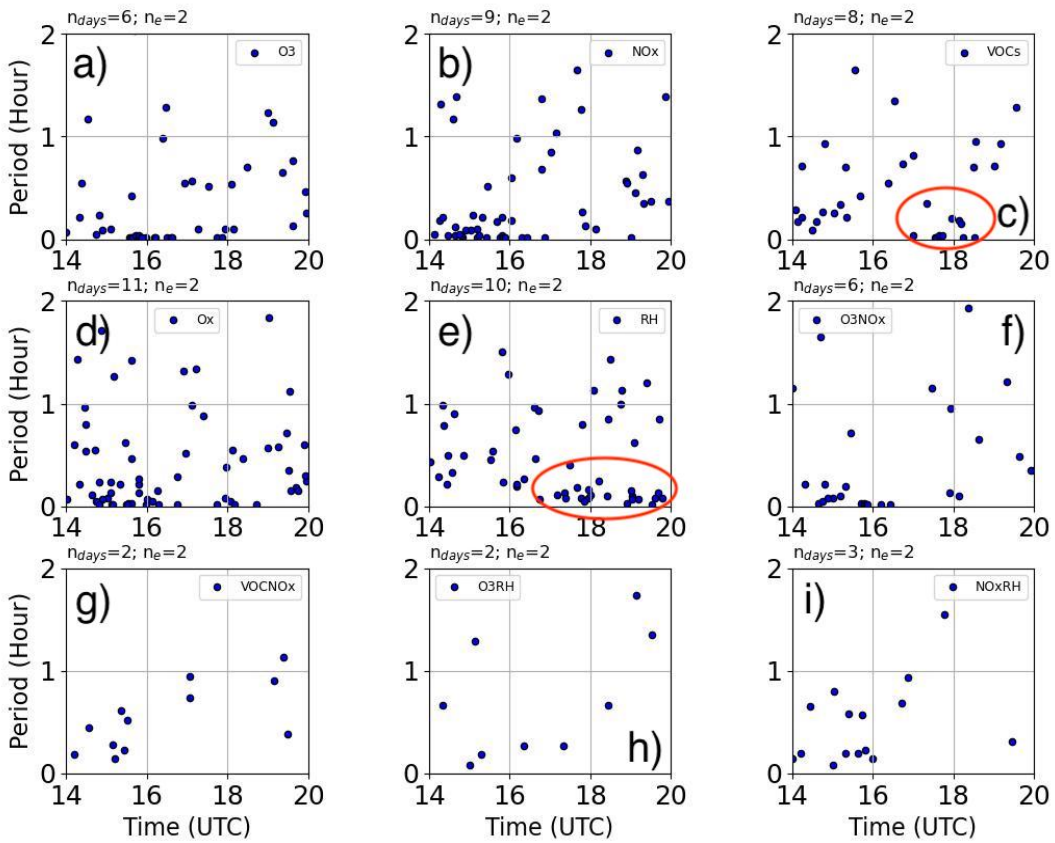

Figure 11. Time (x-axis) versus temporal width of extremum (τ_{max}–y-axis) for a) O_3, b) NO_x, c) VOCs, d) O_x, e) surface relative humidity, f) O_3&NO_x, g) VOCs&NO_x, h) O_3&relative humidity, and i) NO_x&relative humidity. Each panel includes a subtitle with the number of days (n_{days}) and the number of O_3 exceedance days (n_e). Red ovals are included for variables that exhibit high frequency variability spanning the time period that a SB was typically observed based on subjective identification.

BL heights (> 1 hour) approximately leads to a slope that is 0.027 m s^{-1} (not shown), which agrees with what was found in the 16 August case study. It is also clear that high frequency variability is evident in O_3 (Figure 12a) on the order of 5 minutes when the BL height is between 250 and 500 m. Though we did not subjectively identify the high frequency scatter in Figure 11a (many of these high frequency scatter fell between 15 (8 PT) and 17 (10 PT) UTC), we do recognize the possibility that the high frequency variability observed at this time could be related to an early onset arrival of a SB, other dynamical interactions unaccounted for, or rapid chemical reactions with O_3 precursors. Outside of the high frequency variability in Figure 12a, the temporal width of extremum for O_3 does increase with BL height, but unlike most other variables, the number of days is weighted towards non-exceedance events. Variable pairings in Figure 12g-h show an increase in the temporal width

https://doi.org/10.5194/egusphere-2024-447
Preprint. Discussion started: 5 April 2024

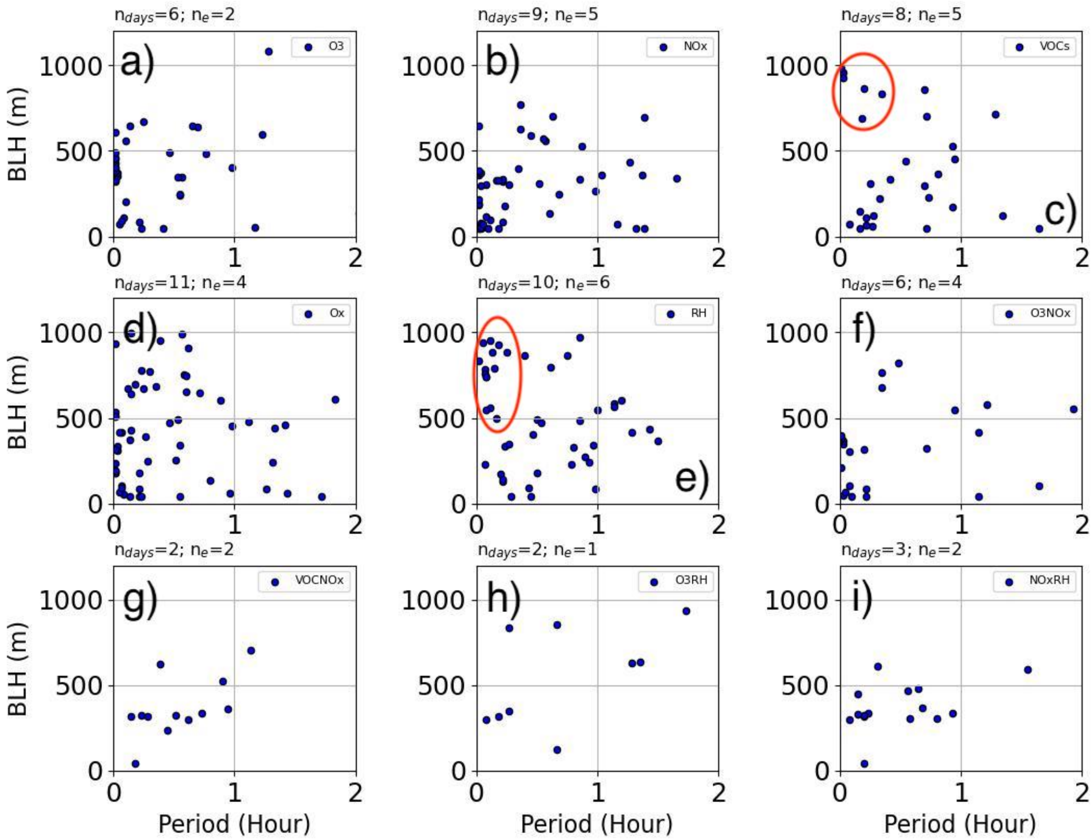

Figure 12. The time-scales associated with extrema on scaleograms (τ_{max}–x-axis) versus BL height (y-axis) for a) O_3, b) NO_x, c) VOCs, d) O_x, e) surface relative humidity, f) O_3&NO_x, g) VOCs&NO_x, h) O_3&relative humidity, and i) NO_x&relative humidity. Each panel includes a subtitle with the number of days (n_{days}) and the number of O_3 exceedance days (n_e). Red ovals are included for variables that exhibit high frequency variability spanning the time period that the SB was typically observed based on subjective identification.

of extremum with BL height, especially for NO_x&VOCs; but again, the number of days identified was 2, which represents a dimunitive sample size.

It is interesting to note the stronger dependence of increased temporal width of extremum with BL growth for NO_x and VOCs compared to other variables. Though not as robust as findings from the case study presented, the general increasing trends points to the importance of convection and entrainment during the BL growth phase that modifies the volume of interaction and leads to a time evolution of air quality measurements at the surface that can be at least partially attributable to the dynamics. Re-examining Figures 2 and 4, it is clear that VOCs retained high concentrations throughout the morning and afternoon compared to NO_x on O_3 exceedance days, but that all three featured increases in the temporal width of extremum with respect to BL growth, especially for NO_x and VOCs. The growth of the BL increases the volume over which pollutants get distributed, and if pollutants remain relatively stable (e.g., VOCs in Figure 2 and 4), then variations are likely to be dominated by dynamics as a result of increased turnover time-scales that manifest as increases in the temporal width of extremum during BL growth, provided that eddy velocity scales remain relatively constant. It is important to note that other dynamical contributing factors and chemical reactions between species that define the NO_x and RO_x cycles have a non-negligible contribution to the evolution, and thus more work would need to be done with a longer continuous data record and with increased temporal resolution of dynamics measurements to exploit the relationship between dynamics and chemistry more decisively.

6 Conclusions

In this study, we presented data collected during the Southwest Urban NO_x and VOCs Experiment (SUNVEx) to understand the role of multi-scaled dynamics in Pasadena, CA located within the LA basin during August 2021. About half the days experienced O_3 exceeding 70 ppb that coincided with elevated $PM_{2.5}$, increased NO_x during nights preceding O_3 exceedance, and increased VOCs into the afternoon hours. Time versus date curtain plots also revealed increased temperature, reduced relative humidty, and lower daytime BL heights during days where $O_3 \geq 70$ ppb. Separating the data into exceedance and no exceedance categories highlighted increased surface pressure, reduced winds, and lower BL heights as being favorable conditions for elevated (lowered) O_3 during the day (night). At nighttime, shallower BL heights, reduced winds, and reduced surface temperature led to increased static stability and stagnation that was responsible for the build-up of pollutants as observed in NO_x and VOCs. The shallower BL height during daytime for O_3 exceedance days was likely a combination of reduced winds (less mechanical production of turbulence across the BL) and modifications to the thermodynamic structure above the BL inversion as subsidence during high pressure situations can lead to increased temperatures that strengthen the inversion. These results contrast with days where O_3 did not reach 70 ppb, which instead featured increased BL heights at night as a result of increased wind shear and stronger winds that can reduce the role of titration at removing O_3, and increased BL heights and BL-averaged wind during the day which can dilute daytime concentrations, thereby altering the volume by which pollutants interact. While the wind direction was markedly different at night between days where O_3 exceeded 70 ppb (northerly to northeasterly) versus days when O_3 did not exceed 70 ppb (southerly to southeasterly), the wind direction converged to southwesterly during the daytime, which typically coincided with increased wind speed as the marine BL propagated inland. An interesting meteorological feature worth noting was the semi-diurnal pressure pattern, whose troughs lined up near transitional periods (sunset and sunrise) and coincided with the timing of wind direction shifts above the BL (e.g., Figure 6b).

To evaluate micrometeorological impacts on air quality measurements, 16 August was chosen to study the rapid changes in chemical concentrations from sunrise into late afternoon with the arrival of a SB. Winds across the BL were relatively weak leading up to sunrise, with a predominately easterly flow in the evening near the surface that gave way to southwesterly flows into the afternoon. A diurnal pattern in wind direction above the BL was evident by northerly flows during the night that transitioned to easterly flows during the day. Patterns of descent throughout the evening were also evident in the wind direction and wind speed as shown by arrows in Figure 6a-b. As the BL depth increased during the day, the winds that descended from

https://doi.org/10.5194/egusphere-2024-447
Preprint. Discussion started: 5 April 2024

above accelerated. This led to increased wind shear across the top of the BL that coincided with a series of wind speed bursts and developing updrafts that matched with temporal fluctuations in air quality measurements. The descending wind pattern that modified the shear structure also occurred concomitantly with a SB that entered Pasadena. We hypothesize that modifications to the thermodynamic structure of the BL inversion from subsidence led to a shallow wind jet above the BL that initiated entrainment and BL fluctuations as a result of increased stability extending from BL top into a thin layer within the lower free troposphere. Winds were further modified by the SB, thus leading to a very complex wind structure that influenced pollutant concentrations within the BL.

In order to address the precise role of BL dynamics on air quality measurements for the 16 August case study, a method was developed to isolate the fine structure variability of meteorological and air quality measurements from the diurnal trend. Scaleograms were created to understand the spectral characteristics of local time variations within variable time series, while a Multivariate Spectral Coherence Mapping (MSCM) technique was developed and used to combine maximum normalized PSD from different variables to understand variable interdependencies. The fine structure variability of measurements (air quality and dynamics) were most pronounced during BL transitions (i.e., evening transition, at sunrise and throughout the BL growth phase, and during the arrival of the SB). Measurements did not respond uniformly to changes in the BL dynamics. For instance, the fine structure variability in chemical concentrations did not register during the evening transition or throughout the night, while meteorological measurements such as relative humidty, and BL-averaged wind speed and wind speed shear did. Most of the measurements taken at Pasadena exhibited rapid changes during sunrise that ranged from the order of minutes to about an hour. The higher temporal resolution of NO_x and VOC measurements enabled higher frequencies to be examined during BL growth. Both NO_x and VOCs increased as the BL deepened which also corroborated well with variations in the BL structure with respect to time, ranging from 15 minutes shortly after sunrise to 1.5 hours as the BL climaxed. Other measurements did not feature increases in the temporal width of extrema as the BL deepened (i.e., τ_{max} did not increase as the BL deepened). The arrival of the SB coincided with fine structure variability in O_3, NO_x, and O_x that was well correlated. The temporal variability reduced from 30 minutes to about 15 minutes, which approximately matched the temporal spacing between relatively strong updrafts.

Combining two variables using the MSCM technique highlighted the covariability of O_3 and NO_x during the passage of the SB, while strong covariability was observed during the BL growth phase between NO_x, VOCs, and variations in BL height (Figures 8 and 9). Since the temporal width increased with respect to the BL deepening, we conducted a series of powerlaw fits to estimate the analytical structure of τ_{max} and its relation to BL height as justified by the nearly identical values between slopes derived from fitting BL height to τ_{max} ($V_{\tau_{max}}$) and the average rate the BL height deepened (dz_{BL}/dt). While modeling the BL height using Eq. (15) for different variables and variability pairings led to reasonable agreement to the observed BL height, it was found that using τ_{max} from NO_x severely overestimated BL height while using τ_{max} from VOCs and VOCs&NO_x slightly overestimated the BL height until 18.5 UTC (11:30a PT) when the modeled and observed behavior diverged significantly during the arrival of the SB. When the variations in BL height (not the overall trend in BL height) was used with NO_x or VOCs, the modeling of the BL height improved significantly. This shows that while the temporal structure of VOCs and NO_x is well correlated with variations in BL height, that the temporal structure observed in pollutants cannot be

https://doi.org/10.5194/egusphere-2024-447
Preprint. Discussion started: 5 April 2024

explained solely by BL dynamics since the chemistry concentrations (and therefore chemical reaction pathways) are altered in response to an evolving BL. We must stress that the modeling exercise conducted should be viewed more as a thought experiment using some key assumptions in order to see if variations in measurements scaled with BL growth.

Lastly, the entire August 2021 dataset was processed in order to examine whether the case described above was unique or representative. This was done by isolating all days for each variable and variable pairing that had at least four temporal extrema isolated within scaleograms during the BL growth phase for each day. NO_x and VOCs stood out as being most impacted by BL growth as a result of increased temporal width of extremum as the BL height increased. Other variables that consisted of 5 or more days did not feature as strong of a relationship. Subjective elimination of high frequency scatter strengthens the argument that the time-scale of variations in VOCs and NO_x increased with BL growth, while also revealing trends in relative humidity and to some extent O_3. The case presented was unique, but it can be argued that non-linear dynamical and chemistry interactions can lead to a unique set of conditions each day as well, which depend not only on the complex evolution between large-scale, mesoscale, and local (urban heat and wind island effects), but also from stationary and transiting sources of O_3 precursors that make make reproducibility challenging. However, we believe that the results enclosed present a promising method at disentangling the role of dynamics and chemistry on air quality evolution, which we hope to apply to a more continuous dataset in the future that features dynamics measurements at a higher temporal resolution.

6.1 Limitations and Path Forward

A major limitation in this work was the vertical and temporal resolution of the DL. Although we were able to link the dynamics with air quality measurements, the rapid variability in air quality measurements was often at a temporal scale much finer than the 15-minute scan cycle of the DL. Based on the 16 August case study, we believe that a time resolution closer to in situ chemistry measurements would have resulted in stronger relationships between BL-averaged winds and chemistry measurements given the apparent covariability observed between measurements seen in Figure 6, for example. While the vertical resolution of the DL was relatively high (20 m near the surface), a resolution of 20 m across the depth of the profile from a DL or tower measurements with spacing on the order of 5 m near the surface may have improved the diagnosis of the BL height during transitional time periods (i.e., evening and morning transition). The relatively coarse temporal and vertical resolution sometimes led to a discontinuous structure that was not always easy to process via EMD, especially for the BL height product.

Another limitation of the dataset was the relatively short duration over which measurements were taken at Pasadena – only a monthlong dataset. A more continuous record featuring a high temporal resolution dataset (i.e., 60 s time resolution) that spans years so that the same month is covered multiple times will allow stronger statistical relationships to be developed between dynamics and air quality measurements, provided that the resolution of the DL (temporal and vertical) is also improved.

While studies have illustrated the micrometeorological role of BL transitions and SBs on air quality measurements, this study presents a quantiative analysis of the temporal structure observed in both air quality and meteorological measurements as well as the degree to which different variables are correlated. A logical next step would be to extend this analysis with a collocated O_3 lidar to link what is observed at the surface (as done in this study) with O_3 concentrations aloft. This would

https://doi.org/10.5194/egusphere-2024-447
Preprint. Discussion started: 5 April 2024

allow not only a separation of local versus non-local O_3 events, but would allow a link between interactions between pollutants in the BL with pollutants in the free troposphere through entrainment.

Data availability. The data used for this analysis can be found in the Chemical Sciences Laboratory website under (Brewer, 2021) and (S., 2021) for the stationary Doppler lidar and in situ chemistry, respectively, at Pasadena, California.

Appendix A: Ranking Variables With Shared Spectral Characteristics Relative to a Chosen Reference Variable

Suppose we are interested in determining two variables that share similar scaleogram characteristics. We can start with Eq. (8), set $L = 2$ since we are only interested in two variables out of M possible variables, define our reference variable by index m_0, and sort through the remaining $M-1$ variables to examine spectral similarities. Eq. (A1) represents the maximum normalized spectral product between reference variable, x_{m_0}, and the variable that results in maximum spectral coherence, i.e., x_{m_1},

$$\widetilde{C}^2_{m_1} = \left(\widetilde{C}^1_{m_0}\widetilde{\chi}^{m_1}_{\psi}\right)^{\frac{1}{2}} \tag{A1}$$

where $\widetilde{C}^1_{m_0} = \widetilde{\chi}^{m_0}_{\psi}$ by virtue of Eq. (8). The operation in Eq. (A1) results in two variable subspaces: a subspace comprised of the reference variable and the variable selected based on maximum spectral coherence, $\boldsymbol{Y}_1$, and a variable subspace that consists of leftover variables that can be evaluated when maximizing spectral coherence for higher order moments, $\boldsymbol{X}_1$, i.e.,

$$\boldsymbol{Y}_1 = \{x_{m_0}, x_{m_1}\} \tag{A2}$$

and

$$\boldsymbol{X}_1 = \{x_{n_1}, x_{n_2}, ..., x_{n_{M-2}}\} \tag{A3}$$

Here, $\boldsymbol{X}_1 \cap \boldsymbol{Y}_1 = 0$, $\boldsymbol{X}_1 \oplus \boldsymbol{Y}_1 = \boldsymbol{X}$, $\{\boldsymbol{X}_1, \boldsymbol{Y}_1\} \subseteq \boldsymbol{X}$, $\boldsymbol{X} = \{x_{m_0}, x_{m_1}, ..., x_{M_m}\}$, and subscript, n, is a dummy placeholder to denote the remaining $M-2$ variables that can be selected if we were to maximize spectral coherence for a third moment calculation. It should be noted that index, m_1, could pertain to any variable within the list of available variables (i.e., $\boldsymbol{X}_0 = \{x_{n_1}, x_{n_2}, ..., x_{n_{M-1}}\}$), where $x_{m_0} \notin \boldsymbol{X}_0$.

If we take the result from Eq. (A1) and sort through the remaining variables in Eq. (A3), we can isolate the variable that would maximize spectral coherence for a third moment calculation ($L = 3$), i.e.,

$$\widetilde{C}^3_{m_2} = \left(\widetilde{C}^2_{m_1}\right)^{\frac{2}{3}}\left(\widetilde{\chi}^{m_2}_{\psi}\right)^{\frac{1}{3}} \rightarrow \left(\widetilde{C}^1_{m_0}\widetilde{\chi}^{m_1}_{\psi}\widetilde{\chi}^{m_2}_{\psi}\right)^{\frac{1}{3}} \tag{A4}$$

thus leading to a reduced variable subspace of remaining variables that can be selected, i.e., $\boldsymbol{X}_2$, and an inflated variable subspace comprised of selected variables, $\boldsymbol{Y}_2$, i.e.,

$$\boldsymbol{X}_2 = \{x_{n_1}, x_{n_2}, ..., x_{n_{M-3}}\} \tag{A5}$$

https://doi.org/10.5194/egusphere-2024-447
Preprint. Discussion started: 5 April 2024

and

$$\boldsymbol{Y}_2 = \{x_{m_0}, x_{m_1}, x_{m_2}\} \tag{A6}$$

As before, the following conditions apply, but this time to Equations (A5) and (A6): i.e., $\boldsymbol{X}_2 \cap \boldsymbol{Y}_2 = 0$, $\boldsymbol{X}_2 \oplus \boldsymbol{Y}_2 = \boldsymbol{X}$, and $\{\boldsymbol{X}_2, \boldsymbol{Y}_2\} \subseteq \boldsymbol{X}$.

Following this progression, we can define a fourth moment (i.e., $L = 4$) along with the following variable subspaces, i.e.,

$$\widetilde{C}^4_{m_3} = \left(\widetilde{C}^3_{m_2}\right)^{\frac{3}{4}} \left(\widetilde{\chi}^{m_3}_{\psi}\right)^{\frac{1}{4}} \to \left(\widetilde{C}^1_{m_0} \widetilde{\chi}^{m_1}_{\psi} \widetilde{\chi}^{m_2}_{\psi} \widetilde{\chi}^{m_3}_{\psi}\right)^{\frac{1}{4}} \tag{A7}$$

$$\boldsymbol{X}_3 = \{x_{n_1}, x_{n_2}, ..., x_{n_{M-4}}\} \tag{A8}$$

$$\boldsymbol{Y}_3 = \{x_{m_0}, x_{m_1}, x_{m_2}, x_{m_3}\} \tag{A9}$$

As can be seen, the sequence of operations outlined above can be extended into general terms, i.e.,

$$\widetilde{C}^L(\tau, b) = \left(\prod_{j=1}^{L} \widetilde{\chi}^j_{\psi}(\tau, b)\right)^{1/L} \tag{A10}$$

where the following conditions are satisfied regardless of the moment order, i.e.,

$$\{\boldsymbol{X}_0 \cap \boldsymbol{Y}_0, \boldsymbol{X}_1 \cap \boldsymbol{Y}_1, ..., \boldsymbol{X}_M \cap \boldsymbol{Y}_M\} = 0 \tag{A11}$$

$$\{\boldsymbol{X}_0 \oplus \boldsymbol{Y}_0, \boldsymbol{X}_1 \oplus \boldsymbol{Y}_1, ..., \boldsymbol{X}_M \oplus \boldsymbol{Y}_M\} = \boldsymbol{X} \tag{A12}$$

Lastly, as the moment order approaches the number of available variables, the inflated variable subspace converges to $\boldsymbol{X}$, i.e.,

$$\lim_{L \to M} \boldsymbol{Y}_L = \boldsymbol{X} \tag{A13}$$

The additional benefit of the approach outlined above is that the variables are automatically ordered based on the degree of spectral simiilarity with the reference variable regardless of the number of variables used in the operational sequence, thus leading to the ranking of variables with respect to an arbitrary reference variable.

Appendix B: Derivation of BL Height Using Maximum Periods Determined from scaleograms

Instead of equating the time derivative of the BL height to Eq. (12) as was done in Eq. (13), let us take the time derivative of Eq. (12) directly, i.e.,

$$\frac{dV_{\tau_{max}}}{dt} = \frac{d}{dt}\left(\frac{z_{BL}}{\tau_{max}}\right) \to \frac{1}{\tau_{max}} \frac{dz_{BL}}{dt} - \frac{z_{BL}}{\tau^2_{max}} \frac{d\tau_{max}}{dt} \tag{B1}$$

https://doi.org/10.5194/egusphere-2024-447
Preprint. Discussion started: 5 April 2024

From there, we can divide Eq. (B1) by $V_{\tau_{max}}$

$$\frac{d\ln V_{\tau_{max}}}{dt} = \frac{1}{V_{\tau_{max}}\tau_{max}}\frac{dz_{BL}}{dt} - \frac{z_{BL}}{V_{\tau_{max}}\tau_{max}^2}\frac{d\tau_{max}}{dt} \tag{B2}$$

and substitute $V_{\tau_{max}}$ for z_{BL}/τ_{max} into the right hand side of Eq. (B2), followed by a series of cancellations, i.e.,

$$\frac{d\ln V_{\tau_{max}}}{dt} = \frac{d\ln z_{BL}}{dt} - \frac{d\ln \tau_{max}}{dt} \tag{B3}$$

The remaining terms can be merged with the time derivative of variables to simplify the form into the time derivative of the natural log of variables (Eq. (B3)). We can now integrate Eq. (B3) with respect to time, which leads to

$$\int_{\ln V_{\tau_{max}}(t_0)}^{\ln V_{\tau_{max}}(t)} d\ln V_{\tau_{max}} = \int_{\ln z_{BL}(t_0)}^{\ln z_{BL}(t)} d\ln z_{BL} - \int_{\ln \tau_{max}(t_0)}^{\ln \tau_{max}(t)} d\ln \tau_{max} \tag{B4}$$

where t_0 refers to the time at sunrise while t is some arbitrary time during the growth phase of the BL. Carrying out the integration in Eq. (B4) leads to

$$\ln\left(\frac{V_{\tau_{max}}(t)}{V_{\tau_{max}}(t_0)}\right) = \ln\left(\frac{z_{BL}(t)}{z_{BL}(t_0)}\right) - \ln\left(\frac{\tau_{max}(t)}{\tau_{max}(t_0)}\right) \tag{B5}$$

Taking the exponential of Eq. (B5) and subsituting in $V_{\tau_{max}}(t)$=$z_{BL}(t)/\tau_{max}(t)$ and $V_{\tau_{max}}(t_0)$=$z_{BL}(t_0)/\tau_{max}(t_0)$ results in

$$\frac{z_{BL}(t)}{\tau_{max}(t)}\frac{\tau_{max}(t_0)}{z_{BL}(t_0)} = \frac{z_{BL}(t)}{z_{BL}(t_0)} - \frac{\tau_{max}(t)}{\tau_{max}(t_0)} \tag{B6}$$

which can then be manipulated to isolate $z_{BL}(t)$, i.e.,

$$z_{BL}(t) = z_{BL}(t_0)\frac{\tau_{max}(t)}{\tau_{max}(t_0)}\left(1 - \frac{\tau_{max}(t_0)}{\tau_{max}(t)}\right)^{-1} \tag{B7}$$

A major shortcoming of Eq. (B7) is the blow-up that occurs at sunrise when t=t_0. However, if we recall that the fits to derive slopes in Figure 10b were done against data that was well correlated, and that the slope suggests a nearly constant velocity, then we can assume that $dV_{\tau_{max}}/dt$=0 such that Eq. (B7) simplifies to

$$z_{BL}(t) \approx z_{BL,0}\frac{\tau_{max}(t)}{\tau_{max,0}} \tag{B8}$$

Here, Eq. (B8) represents the analytical relation used to model BL heights with derived τ_{max}'s in Figure 10c. Although a tedious exercise, Eq. (B8) assumes that the BL height can be modeled using changes in the temporal structure if the initial conditions at sunrise for both BL height and τ_{max} are known. Furthermore, the form of $\tau_{max}(t)$ is represented as a general function, but as determined by the variable and variable pairings selected for Figure 10, follows a powerlaw behavior. We suspect that this form could be potentially used to separate the dynamical influence of BL growth from advection and chemical reactions that would also change the temporal characteristics of air quality measurements.

https://doi.org/10.5194/egusphere-2024-447
Preprint. Discussion started: 5 April 2024

Author contributions. EJS conceptualized, conducted the scientific analysis, and drafted the manuscript. SB and BJC helped with the focus and writing of the manuscript, and participated in discussions on the analysis. SSB assisted with improved focus and messaging related to explanations tied to the chemistry. KZ improved the messaging and focus of the manuscript, suggested a deeper dive into in situ pressure measurements, and incorporated Section 2.1.2. MC assisted with the messaging and writing of manuscript, and incorporated Section 2.1.3. AWB, LX, YLP, and CES assisted with the messaging and writing of the manuscript. CW, JP, JG, BM, MH, and RM were involved in data acquisition and curation.

Competing interests. At least one of the (co-)authors is a member of the editorial board of Atmospheric Chemistry and Physics

Acknowledgements. The corresponding author would like to acknowledge the careful attention and involvement of co-authors which led to significant improvements in the focus and messaging of the manuscript. The authors are grateful for the feedback and stimulating discussions from reviewers.

References

Baidar, S., Bonin, T., Choukulkar, A., Brewer, A., and Hardesty, M.: Observation of the urban wind island effect, in: EPJ Web of Conferences, vol. 237, p. 06009, EDP Sciences, 2020.

Banta, R., Senff, C., Nielsen-Gammon, J., Darby, L., Ryerson, T., Alvarez, R., Sandberg, S., Williams, E., and Trainer, M.: A bad air day in Houston, Bulletin of the American Meteorological Society, 86, 657–670, 2005.

Bonin, T. A., Carroll, B. J., Hardesty, R. M., Brewer, W. A., Hajny, K., Salmon, O. E., and Shepson, P. B.: Doppler lidar observations of the mixing height in Indianapolis using an automated composite fuzzy logic approach, Journal of Atmospheric and Oceanic Technology, 35, 473–490, 2018.

Brewer, W. A.: Doppler Lidar Observations Stationed at Pasadena, California During SUNVEx, https://csl.noaa.gov/groups/csl3/measurements/2021sunvex/dalek01/, 2021.

Coggon, M. M., Stockwell, C. E., Claflin, M. S., Pfannerstill, E. Y., Lu, X., Gilman, J. B., Marcantonio, J., Cao, C., Bates, K., Gkatzelis, G. I., et al.: Identifying and correcting interferences to PTR-ToF-MS measurements of isoprene and other urban volatile organic compounds, EGUsphere, 2023, 1–41, 2023.

de Gouw, J. d., Gilman, J., Kim, S.-W., Lerner, B., Isaacman-VanWertz, G., McDonald, B., Warneke, C., Kuster, W., Lefer, B., Griffith, S., et al.: Chemistry of volatile organic compounds in the Los Angeles basin: Nighttime removal of alkenes and determination of emission ratios, Journal of Geophysical Research: Atmospheres, 122, 11–843, 2017.

Dowell, D. C., Alexander, C. R., James, E. P., Weygandt, S. S., Benjamin, S. G., Manikin, G. S., Blake, B. T., Brown, J. M., Olson, J. B., Hu, M., et al.: The High-Resolution Rapid Refresh (HRRR): An hourly updating convection-allowing forecast model. Part I: Motivation and system description, Weather and Forecasting, 37, 1371–1395, 2022.

Droste, A. M., Steeneveld, G.-J., and Holtslag, A. A.: Introducing the urban wind island effect, Environmental Research Letters, 13, 094 007, 2018.

Fuchs, H., Dubé, W. P., Lerner, B. M., Wagner, N. L., Williams, E. J., and Brown, S. S.: A sensitive and versatile detector for atmospheric NO2 and NOx based on blue diode laser cavity ring-down spectroscopy, Environmental science & technology, 43, 7831–7836, 2009.

Grinsted, A., Moore, J. C., and Jevrejeva, S.: Application of the cross wavelet transform and wavelet coherence to geophysical time series, Nonlinear processes in geophysics, 11, 561–566, 2004.

Gu, S., Guenther, A., and Faiola, C.: Effects of anthropogenic and biogenic volatile organic compounds on Los Angeles air quality, Environmental Science & Technology, 55, 12 191–12 201, 2021.

Hansen, R., Griffith, S., Dusanter, S., Gilman, J., Graus, M., Kuster, W., Veres, P., de Gouw, J., Warneke, C., Washenfelder, R., et al.: Measurements of Total OH Reactivity During CalNex-LA, Journal of Geophysical Research: Atmospheres, 126, e2020JD032 988, 2021.

Hasheminassab, S., Daher, N., Ostro, B. D., and Sioutas, C.: Long-term source apportionment of ambient fine particulate matter (PM2. 5) in the Los Angeles Basin: A focus on emissions reduction from vehicular sources, Environmental Pollution, 193, 54–64, 2014.

Huang, N. E. and Wu, Z.: A review on Hilbert-Huang transform: Method and its applications to geophysical studies, Reviews of geophysics, 46, 2008.

Krechmer, J., Lopez-Hilfiker, F., Koss, A., Hutterli, M., Stoermer, C., Deming, B., Kimmel, J., Warneke, C., Holzinger, R., Jayne, J., et al.: Evaluation of a new reagent-ion source and focusing ion–molecule reactor for use in proton-transfer-reaction mass spectrometry, Analytical chemistry, 90, 12 011–12 018, 2018.

https://doi.org/10.5194/egusphere-2024-447
Preprint. Discussion started: 5 April 2024

Lai, L.-W. and Cheng, W.-L.: Air quality influenced by urban heat island coupled with synoptic weather patterns, Science of the total environment, 407, 2724–2733, 2009.

Langford, A., Senff, C., Alvarez, R., Banta, R., and Hardesty, R.: Long-range transport of ozone from the Los Angeles Basin: A case study, Geophysical Research Letters, 37, 2010.

Loughner, C. P., Tzortziou, M., Follette-Cook, M., Pickering, K. E., Goldberg, D., Satam, C., Weinheimer, A., Crawford, J. H., Knapp, D. J., Montzka, D. D., et al.: Impact of bay-breeze circulations on surface air quality and boundary layer export, Journal of Applied Meteorology and Climatology, 53, 1697–1713, 2014.

Lu, R. and Turco, R. P.: Air pollutant transport in a coastal environment—II. Three-dimensional simulations over Los Angeles basin, Atmospheric Environment, 29, 1499–1518, 1995.

McDonald, B. C., De Gouw, J. A., Gilman, J. B., Jathar, S. H., Akherati, A., Cappa, C. D., Jimenez, J. L., Lee-Taylor, J., Hayes, P. L., McKeen, S. A., et al.: Volatile chemical products emerging as largest petrochemical source of urban organic emissions, Science, 359, 760–764, 2018.

Muñiz-Unamunzaga, M., Borge, R., Sarwar, G., Gantt, B., de la Paz, D., Cuevas, C. A., and Saiz-Lopez, A.: The influence of ocean halogen and sulfur emissions in the air quality of a coastal megacity: The case of Los Angeles, Science of The Total Environment, 610, 1536–1545, 2018.

Nauth, D., Loughner, C. P., and Tzortziou, M.: The Influence of Synoptic-Scale Wind Patterns on Column-Integrated Nitrogen Dioxide, Ground-Level Ozone, and the Development of Sea-Breeze Circulations in the New York City Metropolitan Area, Journal of Applied Meteorology and Climatology, 62, 645–655, 2023.

Nussbaumer, C. M. and Cohen, R. C.: The role of temperature and NO x in ozone trends in the Los Angeles Basin, Environmental Science & Technology, 54, 15 652–15 659, 2020.

Nussbaumer, C. M. and Cohen, R. C.: Impact of OA on the Temperature Dependence of PM 2.5 in the Los Angeles Basin, Environmental Science & Technology, 55, 3549–3558, 2021.

Parrish, D. D., Xu, J., Croes, B., and Shao, M.: Air quality improvement in Los Angeles—Perspectives for developing cities, Frontiers of Environmental Science & Engineering, 10, 1–13, 2016.

Pérez, I. A., García, M. Á., Sánchez, M. L., Pardo, N., and Fernández-Duque, B.: Key points in air pollution meteorology, International Journal of Environmental Research and Public Health, 17, 8349, 2020.

Peterson, D. A., Hyer, E. J., Han, S.-O., Crawford, J. H., Park, R. J., Holz, R., Kuehn, R. E., Eloranta, E., Knote, C., Jordan, C. E., et al.: Meteorology influencing springtime air quality, pollution transport, and visibility in Korea, Elem Sci Anth, 7, 57, 2019.

Pusede, S., Gentner, D., Wooldridge, P., Browne, E., Rollins, A., Min, K.-E., Russell, A., Thomas, J., Zhang, L., Brune, W., et al.: On the temperature dependence of organic reactivity, nitrogen oxides, ozone production, and the impact of emission controls in San Joaquin Valley, California, Atmospheric Chemistry and Physics, 14, 3373–3395, 2014.

Rollins, A. W., Rickly, P. S., Gao, R.-S., Ryerson, T. B., Brown, S. S., Peischl, J., and Bourgeois, I.: Single-photon laser-induced fluorescence detection of nitric oxide at sub-parts-per-trillion mixing ratios, Atmospheric Measurement Techniques, 13, 2425–2439, 2020.

Ryerson, T., Andrews, A., Angevine, W., Bates, T., Brock, C., Cairns, B., Cohen, R., Cooper, O., De Gouw, J., Fehsenfeld, F., et al.: The 2010 California research at the Nexus of air quality and climate change (CalNex) field study, Journal of Geophysical Research: Atmospheres, 118, 5830–5866, 2013.

S., B. S.: In Situ Observations Stationed at Pasadena, California During SUNVEx, https://csl.noaa.gov/groups/csl7/measurements/2021sunvex/GroundLA/DataDownload/, 2021.

https://doi.org/10.5194/egusphere-2024-447
Preprint. Discussion started: 5 April 2024

Sastre, M., Yagüe, C., Román-Cascón, C., and Maqueda, G.: Atmospheric boundary-layer evening transitions: a comparison between two different experimental sites, Boundary-Layer Meteorology, 157, 375–399, 2015.

Schroeder, P., Brewer, W. A., Choukulkar, A., Weickmann, A., Zucker, M., Holloway, M. W., and Sandberg, S.: A compact, flexible, and robust micropulsed Doppler lidar, Journal of Atmospheric and Oceanic Technology, 37, 1387–1402, 2020.

Seinfeld, J. H. and Pandis, S. N.: Atmospheric chemistry and physics: from air pollution to climate change, John Wiley & Sons, 2016.

Sekimoto, K., Li, S.-M., Yuan, B., Koss, A., Coggon, M., Warneke, C., and de Gouw, J.: Calculation of the sensitivity of proton-transfer-reaction mass spectrometry (PTR-MS) for organic trace gases using molecular properties, International Journal of Mass Spectrometry, 421, 71–94, 2017.

Strobach, E., Brewer, W., Senff, C., Baidar, S., and McCarty, B.: Isolating and Investigating Updrafts Induced by Wildland Fires Using an Airborne Doppler Lidar During FIREX-AQ, Journal of Geophysical Research: Atmospheres, 128, e2023JD038 809, 2023.

Wagner, N., Riedel, T., Roberts, J., Thornton, J., Angevine, W., Williams, E., Lerner, B., Vlasenko, A., Li, S., Dube, W., et al.: The sea breeze/land breeze circulation in Los Angeles and its influence on nitryl chloride production in this region, Journal of Geophysical Research: Atmospheres, 117, 2012.

Wang, L., Liu, J., Gao, Z., Li, Y., Huang, M., Fan, S., Zhang, X., Yang, Y., Miao, S., Zou, H., et al.: Vertical observations of the atmospheric boundary layer structure over Beijing urban area during air pollution episodes, Atmospheric Chemistry and Physics, 19, 6949–6967, 2019.

Wang, T., Xue, L., Brimblecombe, P., Lam, Y. F., Li, L., and Zhang, L.: Ozone pollution in China: A review of concentrations, meteorological influences, chemical precursors, and effects, Science of the Total Environment, 575, 1582–1596, 2017.

Warneke, C., De Gouw, J. A., Holloway, J. S., Peischl, J., Ryerson, T. B., Atlas, E., Blake, D., Trainer, M., and Parrish, D. D.: Multiyear trends in volatile organic compounds in Los Angeles, California: Five decades of decreasing emissions, Journal of Geophysical Research: Atmospheres, 117, 2012.

Washenfelder, R., Wagner, N., Dube, W., and Brown, S.: Measurement of atmospheric ozone by cavity ring-down spectroscopy, Environmental science & technology, 45, 2938–2944, 2011.

Wild, R. J., Dubé, W. P., Aikin, K. C., Eilerman, S. J., Neuman, J. A., Peischl, J., Ryerson, T. B., and Brown, S. S.: On-road measurements of vehicle NO2/NOx emission ratios in Denver, Colorado, USA, Atmospheric Environment, 148, 182–189, 2017.

Yoon-Hee, K., Song, S.-K., Hwang, M.-K., Jeong, J.-H., and Yoo-Keun, K.: Impacts of detailed land-use types and urban heat in an urban canopy model on local meteorology and ozone levels for air quality modeling in a coastal city, Korea, TAO: Terrestrial, Atmospheric and Oceanic Sciences, 27, 8, 2016.

Zhang, H., Wang, Y., Park, T.-W., and Deng, Y.: Quantifying the relationship between extreme air pollution events and extreme weather events, Atmospheric Research, 188, 64–79, 2017.

Zhou, C., Wei, G., Xiang, J., Zhang, K., Li, C., and Zhang, J.: Effects of synoptic circulation patterns on air quality in Nanjing and its surrounding areas during 2013–2015, Atmospheric Pollution Research, 9, 723–734, 2018.